# A computationally efficient 2D model for inherently equilibrated 3D stress predictions in heterogeneous laminated plates. Part II: Model validation

R.M.J. Groh[a,*], P.M. Weaver[a]

[a] *Advanced Composites Centre for Innovation and Science, University of Bristol, Queen's Building, University Walk, Bristol, BS8 1TR, UK*

**Abstract**

The higher-order, equivalent single-layer model developed in *Part I* is applied to the stretching and bending of exemplar multilayered flat plates, where the results are compared with different 3D models, and trends and insights are subsequently drawn. The present mixed displacement/stress-based model is derived from inherently equilibrated 3D stress fields that satisfy the interlaminar and surface traction equilibrium conditions. A new set of governing equations is derived from a contracted Hellinger-Reissner functional that only enforces the classical membrane and bending equations via Lagrange multipliers. Combined with the fact that the same set of stress resultants is used for all stress fields, the number of unknown variables of the theory reduces, while maintaining sufficient fidelity to capture higher-order transverse shearing and zig-zag effects. A wide range of stacking sequences are considered ranging from orthotropic straight-fibre laminates to sandwich panels with variable-stiffness face sheets, i.e. composite plies in which the reinforcing fibres describe curvilinear paths. Hence, the model is used to study laminated plates with *3D heterogeneity*, that is laminates comprising layers with material properties that can differ by multiple orders of magnitude and that vary continuously in-plane. The governing equations are solved both analytically using trigonometric expansions and numerically using the pseudo-spectral differential quadrature method. The 3D stress fields predictions correlate closely with 3D elasticity and 3D finite element solutions and are accurate to within a few percent for thick plates with characteristic length to thickness ratios as small as 5:1. In fact, the results suggest that 3D stress fields from our model satisfy Cauchy's 3D equilibrium equations more accurately, and at a three-order degree of freedom reduction in computational cost, compared to high-fidelity 3D FEM models.

*Keywords:* Hellinger-Reissner mixed-variational principle, Variable-stiffness laminated plates, Transverse shear deformation, Zig-zag effects

## 1. Introduction

### *1.1. Hellinger-Reissner model*

In *Part I* [1] of this work, a mixed displacement/stress-based, higher-order zig-zag (ZZ) theory for the bending and stretching of multilayered plates was derived from the Hellinger-Reissner (HR) mixed-variational statement. The model is applicable to multilayered plates of uniform thickness $t$ comprising $N_l$ perfectly bonded laminae with individual thicknesses $t^{(k)}$ (where the superscript $(k)$ refers to properties of the $k^{th}$ layer) as shown in Figure 1. The plies are of arbitrary linear elastic constitution and hence, may be straight-fibre or tow-steered reinforced plastic, foam, honeycomb or other compliant materials. The initial configuration of the plate is referenced in orthogonal Cartesian coordinates $(x, y, z)$ with $x$ and $y$ defining the two in-plane dimensions and $z \in [-t/2, t/2]$ defining the thickness coordinate.

The displacement and stress fields within the domain of the plate are expanded as a Taylor series of the through-thickness coordinate $z$ multiplied by unknown variables defined on the reference surface $\Omega$ coincident with the $(x, y)$-plane. The through-thickness expansion functions are split into global $z$-wise fields to capture transverse shearing effects, and local piecewise-continuous $z$-wise fields to capture the ZZ effect. By using the inverse of the higher-order ABD-matrices, the in-plane stress fields are expressed in terms of layerwise material properties, through-thickness shape functions and a vector of higher-order stress resultants. Hence,

$$\sigma^{(k)} = \begin{Bmatrix} \sigma_x^{(k)} \\ \sigma_y^{(k)} \\ \sigma_{xy}^{(k)} \end{Bmatrix} = \bar{\boldsymbol{Q}}^{(k)} \boldsymbol{f}_\epsilon^{(k)} \boldsymbol{s} \mathcal{F} \tag{1}$$

where $\boldsymbol{s}$ is the inverse of the higher-order ABD-matrix, $\bar{\boldsymbol{Q}}^{(k)}$ is the reduced stiffness matrix assuming plane stress in the $z$-direction, $\boldsymbol{f}_\epsilon^{(k)}$ is an array of through-thickness shapes functions that capture the $z$-wise variations of the in-plane stresses $\sigma^{(k)}$, and $\mathcal{F} = (\mathcal{N}, \mathcal{M}, \dots)$ is a stress

*Corresponding author: rainer.groh@bristol.ac.uk

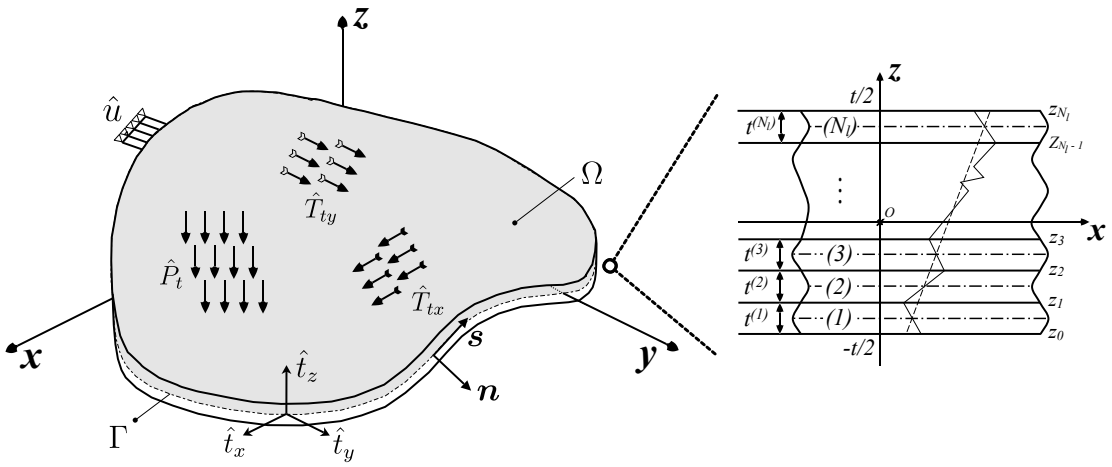


**Figure 1:** A 3D multilayered plate condensed onto an equivalent single layer. The assumed through-thickness displacement field accounts for layerwise ZZ discontinuities which are disregarded in classical theories.

resultants vector defined with respect to the chosen reference surface $\Omega$ and includes the classical membrane stress resultants $\mathcal{N} = (N_x, N_y, N_{xy})$, bending moments $\mathcal{M} = (M_x, M_y, M_{xy})$, and all other higher-order moments. The stress resultants vector is defined by

$$\mathcal{F} = \int_{-t/2}^{t/2} \boldsymbol{f}_{\epsilon}^{(k)^\top} \sigma^{(k)} \mathrm{d}z.$$

Model assumptions for the transverse stresses are derived by integrating the in-plane stresses Eq. (1) in Cauchy's equilibrium equations, and applying interlaminar and surface equilibrium conditions. Hence, the 3D stress field is based on the same set of unknowns $\mathcal{F}$ and is inherently equilibrated. This gives

$$\tau^{(k)} = \begin{Bmatrix} \sigma_{xz}^{(k)} \\ \sigma_{yz}^{(k)} \end{Bmatrix} = \boldsymbol{D}^\top \left[ \left( -\bar{\boldsymbol{Q}}^{(k)} \boldsymbol{g}^{(k)} + \boldsymbol{\alpha}^{(k)} \right) \boldsymbol{s}\mathcal{F} \right] + \hat{T}_b \quad (2)$$

$$\sigma_z^{(k)} = \nabla^\top \boldsymbol{D}^\top \left[ \left\{ \bar{\boldsymbol{Q}}^{(k)} \boldsymbol{h}^{(k)} - \boldsymbol{\alpha}^{(k)} z + \boldsymbol{\beta}^{(k)} \right\} \boldsymbol{s}\mathcal{F} \right] - \nabla^\top \hat{T}_b \left( z - z_0 \right) + \hat{P}_b \quad (3)$$

where $\boldsymbol{g}^{(k)}$ and $\boldsymbol{h}^{(k)}$ are arrays of through-thickness shape functions that capture the $z$-wise variations of the transverse shear stresses $\tau^{(k)}$ and transverse normal stress $\sigma_z^{(k)}$, respectively, and $\boldsymbol{\alpha}^{(k)}$ and $\boldsymbol{\beta}^{(k)}$ enforce the interfacial continuity conditions of $\tau^{(k)}$ and $\sigma_z^{(k)}$, respectively.

Note that $\nabla$ is the del operator and $\boldsymbol{D}^\top$ is a differential operator matrix defined by

$$\boldsymbol{D}^\top = \begin{bmatrix} \dfrac{\partial}{\partial x} & 0 & \dfrac{\partial}{\partial y} \\ 0 & \dfrac{\partial}{\partial y} & \dfrac{\partial}{\partial x} \end{bmatrix}.$$

The governing equations are derived in generalised notation that allows the order of the model to be specified *a priori* without having to re-derive the equations. By integrating all structural properties in the thickness $z$-direction, the model is an equivalent single-layer theory defined in terms of functional unknowns defined on a chosen reference surface $\Omega$, and therefore the total number of variables is independent of the number of layers.

For a certain set of prescribed shear ($\hat{T}$) and normal ($\hat{P}$) tractions $\left(\hat{T}_{bx}, \hat{T}_{by}, \hat{P}_b\right)$ and $\left(\hat{T}_{tx}, \hat{T}_{ty}, \hat{P}_t\right)$ on the bottom ($b$) and top ($t$) surfaces of the 3D body, respectively, the governing field equations derived in [1],

$$\boldsymbol{D}^\top \mathcal{N} + \hat{T}_t - \hat{T}_b = \boldsymbol{0} \quad (4a)$$

$$\nabla^\top \boldsymbol{D}^\top \mathcal{M} + \nabla^\top \left( z_{N_l} \hat{T}_t - z_0 \hat{T}_b \right) + \hat{P}_t - \hat{P}_b = 0 \quad (4b)$$

$$\left( \boldsymbol{s} + \boldsymbol{\eta} \right) \mathcal{F} + \boldsymbol{\eta}_x \frac{\partial \mathcal{F}}{\partial x} + \boldsymbol{\eta}_y \frac{\partial \mathcal{F}}{\partial y} + \boldsymbol{\eta}_{xx} \frac{\partial^2 \mathcal{F}}{\partial x^2} + \boldsymbol{\eta}_{xy} \frac{\partial^2 \mathcal{F}}{\partial x \partial y} + \boldsymbol{\eta}_{yy} \frac{\partial^2 \mathcal{F}}{\partial y^2} + \boldsymbol{\chi} \hat{T}_b + \boldsymbol{\chi}_x \frac{\partial \hat{T}_b}{\partial x} + \boldsymbol{\chi}_y \frac{\partial \hat{T}_b}{\partial y} + \mathcal{L}_{eq} = \boldsymbol{0} \quad (4c)$$

are to be solved for the unknown displacement variables $\boldsymbol{u} = (u_{x_0}, u_{y_0}, w_0)$, i.e. the in-plane and transverse displacements of the equivalent single layer in Cartesian $(x, y, z)$-coordinates, and the stress resultants vector $\mathcal{F}$. Eqs. (4a) and (4b) are the classical membrane and bending equilibrium equations, respectively. Eq. (4c) represents an "enhanced" constitutive relation between the reference surface strains $\epsilon_0$, curvatures $\kappa$ and the stress resultants $\mathcal{F}$ taking into account higher-order shearing and zig-zag effects. Thus, the matrices $\boldsymbol{\eta}$ are transverse shear correction factors that, when multiplied by their corresponding higher-order moment derivatives $\dfrac{\partial^n \mathcal{F}}{\partial x_i^n}$, correct the classical reference surface strain, which is defined by the product $\boldsymbol{s}\mathcal{F}$. Similarly, the matrices $\boldsymbol{\chi}$ are correction factors related to the applied surface shear tractions.

When solving the governing field equations Eq. (4), the

pertinent essential and natural boundary conditions

$$\left.\begin{aligned} &\boldsymbol{\eta}^{bc}\mathcal{F} + \boldsymbol{\eta}_x^{bc}\frac{\partial \mathcal{F}}{\partial x} + \boldsymbol{\eta}_y^{bc}\frac{\partial \mathcal{F}}{\partial y} + \boldsymbol{\chi}^{bc}\hat{T}_b + \mathcal{L}_{bc} = \hat{\mathcal{U}}_{bc} \\ &w_0 = \hat{w}_0 \end{aligned}\right\} \text{ on } C_1 \tag{5a}$$

$$\mathcal{F}^*_{bc} = \hat{\mathcal{F}}^*_{bc} \quad \text{and} \quad Q_{nz} = \hat{Q}_{nz} \quad \text{on } C_2 \tag{5b}$$

need to be satisfied on the perimeter curve $\Gamma$ of the equivalent single layer, where this perimeter is split into two disjoint curves $C_1$ and $C_2$ on which displacement and stress resultant boundary conditions are prescribed, respectively. The addition of the superscript $bc$ to any matrix denotes correction factors that are applicable to the boundary curve $\Gamma$, $Q_{nz}$ is the transverse shear force normal to the boundary surface, and $\hat{\mathcal{U}}_{bc}$ is a column vector of prescribed displacement variables on the boundary.

$\mathcal{L}_{eq}$ is a column vector that includes derivatives of the Lagrange multipliers $\boldsymbol{u} = (u_{x_0}, u_{y_0}, w_0)$ and captures the reference surface stretching strains $\epsilon_0$ and curvatures $\kappa$,

$$\mathcal{L}_{eq} = -\begin{bmatrix}\epsilon_0 & \kappa & \mathbf{0}\end{bmatrix}^\top \tag{6}$$

Similarly, $\mathcal{L}_{bc}$ is a column vector that includes the Lagrange multipliers $u_{n_0} = n_x u_{x_0} + n_y u_{y_0}$, $u_{s_0} = -n_y u_{x_0} + n_x u_{y_0}$ and rotations $\dfrac{\partial w_0}{\partial n}$ and $\dfrac{\partial w_0}{\partial s}$ of the boundary perimeter $\Gamma$ in the local normal-tangential $(n, s, z)$-coordinate system, where $\boldsymbol{n} = (n_x, n_y)$ is the outward normal vector to $\Gamma$, i.e.

$$\mathcal{L}_{bc} = \begin{bmatrix} u_{n_0} & u_{s_0} & -\dfrac{\partial w_0}{\partial n} & -\dfrac{\partial w_0}{\partial s} & \mathbf{0}\end{bmatrix}^\top. \tag{7}$$

Detailed derivations and explanations of these governing equations are presented in [1].

### *1.2. Variable-stiffness laminated composites*

*Part I* of this work presented an historic review of displacement-based and mixed-variational 2D equivalent single-layer theories for multilayered plates. Hence, the purpose of this literature review is to briefly introduce the notion of variable-stiffness laminates, which have gained increasing interest over the last decade, and are also modelled within this paper.

Variable-stiffness composites are a promising technology for improving the efficiency of engineering structures due to the increased design space available for tailoring. The idea of tailoring the structural performance of composite laminates by spatially varying the pointwise fibre orientations has been explored since the early 1970's [2]. For example, early work by Hyer and Lee [3] and Hyer and Charette [4] showed that such variable angle tow (VAT) laminates can alleviate stress concentrations around holes by aligning the fibre paths with the directions of principle stress.

In recent years, the use of fibre reinforced composites in primary aircraft structures has led to increased interest in VAT technology. Numerous works have shown that tailoring the in-plane stiffness of a plate allows prebuckling stresses to be redistributed to supported regions, thereby increasing the critical buckling load [5–13]. Specifically, Gürdal et al. [6] have shown that varying the stiffness of the panel perpendicular to the direction of applied end compression results in greater improvements than varying the stiffness in the direction of loading.

Recent results show that VAT plates with linear fibre variations can be designed to exhibit smaller stiffness reductions in the postbuckling regime than their straight-fibre counterparts [14]. In this regard, an interesting application of variable-stiffness technology is in designing cylindrical shells with stable postbuckling paths. It is well known in the engineering community that cylindrical shells are prone to collapse if loaded in axial compression beyond the buckling load. A direct consequence of this postbuckling instability is an extreme sensitivity to initial geometric imperfections and loading conditions, which can lead to actual buckling loads less than 50% of analytical predictions from linear eigenvalue analyses [15]. White and Weaver [16] have recently shown that this imperfection sensitivity can be effectively eliminated, thereby creating stable, plate-like postbuckling responses, by tailoring the fibre paths across the surface of the shell. The idea of introducing flat, plate-like behaviour in shells was also exploited by applying the variable-stiffness concept to decouple the linear membrane-bending coupling characteristic of curved structures [17].

To date, the primary technology for manufacturing VAT laminates is Automated Fibre Placement (AFP), a manufacturing process originally developed in the 1980's to automate lamination of straight fibre laminates. AFP uses a robotic fibre placement head that deposits multiple pre-impregnated tows of "slit-tape" allowing cutting, clamping and restarting of every single tow. However, in AFP, steering is accomplished by bending the tows in-plane which leads to local fibre buckling on the inside radii of the curved tow, and thus limits the steering radius of curvature [18]. Furthermore, if individual tows are placed next to each other by shifting the reference path along a specific direction, tow gaps and overlaps are inevitably required to cover the whole surface.

To overcome the drawbacks of AFP machines, the Continuous Tow Shearing (CTS) technique was developed, which uses shear deformation to steer fibres at the point of application [19]. This technique not only allows much tighter radii of curvature but tow gaps and overlaps are also avoided by tessellating tows on the substrate. In recent characterisation work, Kim et al. [20] showed that CTS can produce impregnation quality similar to commercial pre-preg. One feature of CTS is that in order to maintain the volume fraction of fibre, the thickness of a tow inherently increases as it is sheared. The relation be-

tween unsheared tow thickness $t_0^{(k)}$ and sheared tow thickness $t^{(k)}$ of a layer $k$ is

$$t^{(k)} = \frac{t_0^{(k)}}{\cos\gamma^{(k)}} = t_0^{(k)} \sec\gamma^{(k)} \tag{8}$$

where $\gamma^{(k)}$ is the shearing angle of the tow at the point of application. Consequently, the thickness of a ply may locally increase by a factor of three if the fibre tow is sheared through an angle of 70°.

Whereas a number of works in the literature deal with global structural phenomena of tow-steered composites laminates, such as vibration and buckling, relatively little work has been conducted on higher-order effects in these laminates. Akhavan and Ribeiro [21] and Akhavan et al. [22] investigated the natural modes of vibration and nonlinear bending deflections and stresses of tow-steered composites, respectively, using a Reddy-type third-order shear deformable theory solved via a p-version finite element approach, for a variety of different edge conditions including plates clamped along all four edges. As elucidated in reference [23], the Reddy-type model used by these researchers leads to static inconsistencies for the clamped boundary condition. Furthermore, by being based on a displacement-based theory, the transverse shear stresses were derived by integrating the in-plane stresses in Cauchy's equilibrium equations via a post-processing step. The researchers also point out that tow-steered laminates can be used effectively to tailor deflections and stresses locally, in order to improve damage resistance in certain applications. In further work, Akhavan and Ribeiro [24] extended the vibrational analysis into the nonlinear regime using a first-order model. Coburn et al. [25, 26] accounted for the effect of transverse shear deformation on the buckling behaviour of tow-steered, blade-stiffened wing panels. Akbarzadeh et al. [27] studied the effects of transverse shear deformation on the vibrational and buckling response of moderately thick AFP panels with gaps and overlaps using a Reddy-type third-order shear deformable theory. The authors corroborate the findings of the present authors published in [28] that transverse shear deformation has a bigger impact on tow-steered than straight-fibre laminates. Yazdani and Ribeiro [29] and Yazdani et al. [30] recently published layerwise extensions of the earlier works by Akhavan and co-workers on the free vibration and bending behaviour of tow-steered laminates cited above. Finally, Tornabene et al. [31] studied the free vibrations of doubly curved, variable-stiffness shells using a generalised higher-order model implemented via Carrera's Unified Formulation (CUF) using a local differential quadrature method. Due to the relative novelty of tow-steered laminates, there is little work in the literature on detailed analyses of full 3D stress fields in tow-steered laminates and how these could be tailored to optimise structures for specific objectives. Hence, the present work aims to contribute new insights in this field.

### *1.3. Structure of the paper*

In this work, the derived HR formulation is compared against 3D elasticity and 3D FEM results for a number of straight-fibre and variable-stiffness laminates, as well as sandwich plates. Overall, four different implementations of the HR formulation are considered. The first is a third-order model that does not account for ZZ effects denoted by HR3. The displacement and stress field expansions are truncated after the $z^3$ term such that there are twelve stress resultants in $\mathcal{F}$, the classical membrane forces $\mathcal{N} = (N_x, N_y, N_{xy})$, classical bending moments $\mathcal{M} = (M_x, M_y, M_{xy})$, second-order moments $\mathcal{M}_2 = (M_{2x}, M_{2y}, M_{2xy})$ and third-order moments $\mathcal{M}_3 = (M_{3x}, M_{3y}, M_{3xy})$. Second, the third-order model is enhanced via a ZZ degree of freedom by using either Murakami's zig-zag function (MZZF),

$$\phi^{(k)}_{i_{MZZF}}(z) = (-1)^k \frac{2}{t^{(k)}} \left(z - z_m^{(k)}\right) \quad \text{for} \quad i = x, y \tag{9}$$

where $z_m^{(k)}$ and $t^{(k)}$ are the midplane coordinate and thickness of layer $k$, respectively, or by using the Refined Zig-zag Theory (RZT) function [32],

$$\left.\begin{aligned}
\phi^{(1)}_{i_{RZT}}(x,y,z) &= \left(z + \frac{t}{2}\right)\left(\frac{G_i(x,y)}{G^{(1)}_{iz}(x,y)} - 1\right) \\
\phi^{(k)}_{i_{RZT}}(x,y,z) &= \left(z + \frac{t}{2}\right)\left(\frac{G_i(x,y)}{G^{(k)}_{iz}(x,y)} - 1\right) + \sum_{j=2}^{k} t^{(j-1)}\left(\frac{G_i(x,y)}{G^{(j-1)}_{iz}(x,y)} - \frac{G_i(x,y)}{G^{(k)}_{iz}(x,y)}\right)
\end{aligned}\right\} \text{ for } i = x, y \tag{10}$$

$$\text{and } G_i(x,y) = \left[\frac{1}{t}\sum_{k=1}^{N_l} \frac{t^{(k)}}{G^{(k)}_{iz}(x,y)}\right]^{-1}.$$

For variable-stiffness composites, the RZT ZZ function is not only a layerwise quantity, but also varies with the

in-plane coordinates $(x, y)$ as the transverse shear moduli $G_{iz}^{(k)}(x, y)$ can change from point to point over surface $\Omega$. MZZF on the other hand is invariant of transverse material properties and therefore only varies with location $(x, y)$ when the thickness of the plate changes. In the case of a constant thickness plate, MZZF is purely a layerwise function with $\phi_{x_{MZZF}}^{(k)} = \phi_{y_{MZZF}}^{(k)}$.

When MZZF is used, the model is referred to as HR3-MZZF. When the RZT ZZ function is used, a distinction is made between the original implementation of the RZT ZZ function as defined by Tessler [32], denoted by HR3-RZT, and Gherlone's adaptation [33] that accounts for the presence of externally weak layers (EWLs), which is denoted by HR3-RZTmx, where the mx stands for "modified external". In the RZTmx case, the RZT ZZ function is calculated from modified values of the transverse shear moduli $G_{xz}^{(k)}$ and $G_{yz}^{(k)}$ of layer $k$:

$$\begin{aligned} &\bullet \text{ If } G_{iz}^{(1)} < G_{iz}^{(2)}, \text{ then } G_{iz}^{(1)} = G_{iz}^{(2)}. \\ &\bullet \text{ If } G_{iz}^{(N_l)} < G_{iz}^{(N_l-1)}, \text{ then } G_{iz}^{(N_l)} = G_{iz}^{(N_l-1)}. \end{aligned} \tag{11}$$

where $N_l$ is the total number of layers and $i = x, y$. The rule does not apply if the condition reduces the laminate to have the same transverse shear moduli for all layers, as would be the case for [0/90], [90/0] and [90/0/90] laminates. The ZZ functionality adds three additional ZZ bending moments $\mathcal{M}^\phi = (M_x^\phi, M_y^\phi, M_{xy}^\phi)$ in the case of MZZF, and four in the case of RZT $\mathcal{M}^\phi = (M_x^\phi, M_y^\phi, M_{xy}^\phi, M_{yx}^\phi)$, such that the number of unknowns in $\mathcal{F}$ is increased to fifteen and sixteen, respectively.

The presentation of the results is split into two sections. Section 2 shows the benchmarking results for straight-fibre laminates, whereas Section 3 treats tow-steered laminates. In total, 12 laminates are investigated; four orthotropic straight-fibre laminates, four anisotropic straight-fibre laminates and four tow-steered laminates. For further results, the interested reader is directed to reference [34] and the supplementary online figures submitted with this article. In Section 2.1, orthotropic laminates are compared with Pagano's 3D elasticity solution [35] of an orthotropic plate simply supported along all four edges and loaded by a sinusoidal pressure loading on the top surface. This 3D elasticity solution is not applicable to anisotropic laminates with extension/shear coupling, bend/twist coupling or load cases involving shear tractions applied to the top and bottom surfaces. Therefore, high-fidelity 3D FEM solutions from Abaqus are used to compare more general laminations and load cases in Section 2.2. This second test case considers general anisotropic laminates that are fully clamped along all four edges and loaded by a constant pressure loading and shear traction on the top surface. Similar 3D FEM solutions are used in Section 3.1 to test the accuracy of the model for tow-steered laminates. A large number of different stacking sequences and characteristic in-plane length to width ratios are considered to validate the general applicability of the HR models. Finally, Section 4 draws conclusions and makes suggestions for future work.

## 2. 3D stress fields in straight-fibre laminates and sandwich plates

Consider a square plate of unit in-plane dimensions $a = b = 1$ m and total thickness $t < a, b$. The plate comprises $N_l$ orthotropic, straight-fibre laminae of layer thickness $t^{(k)}$, material stiffness tensor $\boldsymbol{C}^{(k)}$ and fibre orientation $\alpha^{(k)}$. The individual layers can be arranged in any general fashion but are assumed to be perfectly bonded, such that displacement and traction continuity at the interfaces holds. The plate is subjected to certain displacement or traction boundary conditions along its four straight-edge surfaces, e.g. simply supported or rigidly built-in, and is loaded via certain external tractions on the top and bottom surfaces. In reaction to the applied loading and constraining boundary conditions, the plate is assumed to deform isothermally into a new static equilibrium state.

### *2.1. Benchmarking of 3D stresses in orthotropic laminates*

#### *2.1.1. Model implementation*

As a first test, consider the multilayered plate loaded by a sinusoidally distributed pressure load on the top surface and simply supported along all four edges shown in Figure 2. In the HR formulation, the 3D continuum is compressed onto an equivalent single layer $\Omega$ coincident with the midplane of the plate as depicted by the grey surface. All externally applied tractions are zero except for the sinusoidal pressure on the top surface $\hat{P}_t = p_0 \sin(\pi x/a) \sin(\pi y/b)$.

Following Pagano [35], an exact 3D elasticity solution exists for this problem with arbitrary number of orthotropic or isotropic layers, and this is readily implemented in software packages such as MATLAB. Thus, Pagano's solution serves as the benchmark for the orthotropic composite laminates and sandwich plates considered in this section.

For straight-fibre laminates the HR governing field equations (4) are given by

$$\boldsymbol{s}\mathcal{F} + \boldsymbol{\eta}_{xx}\mathcal{F}_{,xx} + \boldsymbol{\eta}_{yy}\mathcal{F}_{,yy} + \boldsymbol{\eta}_{xy}\mathcal{F}_{,xy} + \mathcal{L}_{eq} = \boldsymbol{0} \tag{12a}$$

$$N_{x,x} + N_{xy,y} = 0 \tag{12b}$$

$$N_{xy,x} + N_{y,y} = 0 \tag{12c}$$

$$M_{x,xx} + 2M_{xy,xy} + M_{y,yy} + \hat{P}_t = 0 \tag{12d}$$

where the comma notation is used to denote differentiation, and $N_x, N_y, N_{xy}$ and $M_x, M_y, M_{xy}$ are the classical membrane forces and bending moments, respectively, and are the first six entries in the stress resultant array $\mathcal{F}$.

The simply supported boundary conditions, i.e. each edge can rotate and move normal to its boundary curve

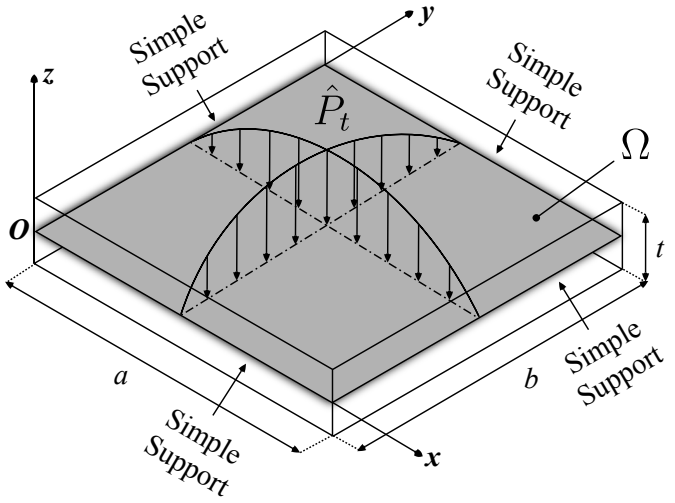


**Figure 2:** A composite plate loaded by a sinusoidally distributed pressure load on the top surface and simply supported along all four edges. In the HR formulation, the 3D continuum is compressed onto an equivalent single layer $\Omega$ coincident with the mid-plane of the plate.

but not tangential to it, are expressed mathematically as

$$\text{at} \quad x = 0, a: \qquad \sigma_x = u_{y_0} = w_0 = 0 \tag{13a}$$
$$\text{at} \quad y = 0, b: \qquad \sigma_y = u_{x_0} = w_0 = 0. \tag{13b}$$

Variable assumptions that satisfy the conditions in Eq. (13), and that are sufficiently general to solve the boundary value problem depicted in Figure 2, are given by

$$\begin{aligned} &u_{x_0} = U\cos\left(\frac{\pi x}{a}\right)\sin\left(\frac{\pi y}{b}\right),\ u_{y_0} = V\sin\left(\frac{\pi x}{a}\right)\cos\left(\frac{\pi y}{b}\right), \\ &(w_0, \mathcal{F}_x, \mathcal{F}_y) = (W, F_{x_0}, F_{y_0})\ \sin\left(\frac{\pi x}{a}\right)\sin\left(\frac{\pi y}{b}\right), \\ &\mathcal{F}_{xy} = F_{xy_0}\cos\left(\frac{\pi x}{a}\right)\cos\left(\frac{\pi y}{b}\right) \end{aligned} \tag{14}$$

where $\mathcal{F}_x = (N_x, M_x, \dots, M_x^\phi)$ are the $x$-wise axial stress resultants, $\mathcal{F}_y = (N_y, M_y, \dots, M_y^\phi)$ are the $y$-wise lateral stress resultants, and $\mathcal{F}_{xy} = (N_{xy}, M_{xy}, \dots, \boldsymbol{M}_{xy}^\phi)$ are the in-plane shear stress resultants. Note that $\boldsymbol{M}_{xy}^\phi$ does not exist for HR3, $\boldsymbol{M}_{xy}^\phi = (M_{xy}^\phi, M_{yx}^\phi)$ for HR3-RZT and $\boldsymbol{M}_{xy}^\phi = M_{xy}^\phi$ for HR3-MZZF.

Substituting Eq. (14) into the governing differential equations (12) results in a set of $N_{eq}$ algebraic equations in $N_{eq}$ variables $(F_{x_0}, F_{y_0}, F_{xy_0}, U, V, W)$, where $N_{eq} = 15$ for HR3, $N_{eq} = 18$ for HR3-MZZF and $N_{eq} = 19$ for HR3-RZT. Note that for orthotropic laminates considered in this problem, the extension/shear coupling stiffness terms $\bar{Q}_{16} = \bar{Q}_{26} = 0$. As a result, all extension/shear and bend/twist coupling terms $s_{ij}$ in the direct compliance matrix $\boldsymbol{s}$ must vanish, i.e. $s_{13} = s_{16} = \cdots = s_{23} = s_{26} = \cdots = s_{31} = s_{32} = s_{34} = s_{35} = \cdots = 0$ because all components in $\boldsymbol{s}$ are linearly dependent on $\bar{\boldsymbol{Q}}$. For the direct shear correction matrix $\boldsymbol{\eta}_{xx}$, the terms associated with $\bar{Q}_{16}$ and $\bar{Q}_{26}$ also vanish, i.e. $\eta_{xx_{13}} = \eta_{xx_{16}} = \cdots = \eta_{xx_{23}} = \eta_{xx_{26}} = \cdots = \eta_{xx_{31}} = \eta_{xx_{32}} = \eta_{xx_{34}} = \eta_{xx_{35}} = \cdots = 0$, and similarly for the direct stiffness matrix $\boldsymbol{\eta}_{yy}$. On the contrary, for the in-plane coupling shear correction matrix $\boldsymbol{\eta}_{xy}$, these aforementioned vanishing terms are the only non-zero values, such that $\eta_{xy_{11}} = \eta_{xy_{12}} = \eta_{xy_{14}} = \eta_{xy_{15}} = \cdots = \eta_{xy_{21}} = \eta_{xy_{22}} = \eta_{xy_{24}} = \eta_{xy_{25}} = \cdots = \eta_{xy_{33}} = \eta_{xy_{36}} = \cdots = 0$.

According to the definition of $\boldsymbol{\eta}_{xx}$ and $\boldsymbol{\eta}_{yy}$ (see Appendix in [1]), these two direct shear correction matrices are functions of the products $\left(\boldsymbol{I}_x\bar{\boldsymbol{Q}}^{(k)}\right)^\top \cdot \left(\boldsymbol{I}_x\bar{\boldsymbol{Q}}^{(k)}\right)$ and $\left(\boldsymbol{I}_y\bar{\boldsymbol{Q}}^{(k)}\right)^\top \cdot \left(\boldsymbol{I}_y\bar{\boldsymbol{Q}}^{(k)}\right)$, respectively, where

$$\boldsymbol{I}_x = \begin{bmatrix} 1 & 0 & 0 \\ 0 & 0 & 1 \end{bmatrix} \text{ and } \boldsymbol{I}_y = \begin{bmatrix} 0 & 0 & 1 \\ 0 & 1 & 0 \end{bmatrix}. \tag{15}$$

The in-plane coupling shear correction matrix $\boldsymbol{\eta}_{xy}$ (see Appendix in [1]), however, is a function of mixed terms $\left(\boldsymbol{I}_x\bar{\boldsymbol{Q}}^{(k)}\right)^\top \cdot \left(\boldsymbol{I}_y\bar{\boldsymbol{Q}}^{(k)}\right) + \left(\boldsymbol{I}_y\bar{\boldsymbol{Q}}^{(k)}\right)^\top \cdot \left(\boldsymbol{I}_x\bar{\boldsymbol{Q}}^{(k)}\right)$. By computing these matrix products involving $\boldsymbol{I}_x, \boldsymbol{I}_y$ and $\bar{\boldsymbol{Q}}^{(k)}$ with $\bar{Q}_{16} = \bar{Q}_{26} = 0$, the set of vanishing shear correction factors above is readily verified.

Thus, in consideration of these vanishing compliance and shear correction terms, and the fact that $a = b = 1\text{m}$, the set of algebraic governing field equations reads

$$\boldsymbol{K}_f F_0 + \boldsymbol{K}_u U_0 = \boldsymbol{0} \tag{16a}$$
$$N_{x_0} - N_{xy_0} = 0 \tag{16b}$$
$$N_{y_0} - N_{xy_0} = 0 \tag{16c}$$
$$\pi^2\left(M_{x_0} + M_{y_0} - 2M_{xy_0}\right) = p_0 \tag{16d}$$

where $F_0 = (N_{x_0}, N_{y_0}, N_{xy_0}, M_{x_0}, M_{y_0}, M_{xy_0}, \dots)$ and $U_0 = (U, V, W)$. The stiffness matrices $\boldsymbol{K}_f$ and $\boldsymbol{K}_u$ multiplying the unknowns $F_0$ and $U_0$ are given by,

$$\boldsymbol{K}_f: \begin{array}{ll} K_{f_{ii}} = s_{ii} - \pi^2\left(\eta_{xx_{ii}} + \eta_{yy_{ii}}\right), & K_{f_{ij}} = \pi^2\eta_{xy_{ij}} \\ K_{f_{ji}} = \pi^2\eta_{xy_{ji}}, & K_{f_{jj}} = s_{jj} - \pi^2\left(\eta_{xx_{jj}} + \eta_{yy_{jj}}\right) \end{array}$$

$$\boldsymbol{K}_u = \begin{bmatrix} \pi & 0 & 0 \\ 0 & \pi & 0 \\ -\pi & -\pi & 0 \\ 0 & 0 & -\pi^2 \\ 0 & 0 & -\pi^2 \\ 0 & 0 & 2\pi^2 \\ 0 & 0 & 0 \\ \vdots & \vdots & \vdots \end{bmatrix}$$

where subscripts $ij$ denote components of the associated

matrices with indices $i$ and $j$ defined by

HR3: $i = (1, 2, 4, 5, \ldots, 10, 11),\ j = (3, 6, \ldots, 12)$
HR3-MZZF: $i = (1, 2, 4, 5, \ldots, 13, 14),\ j = (3, 6, \ldots, 15)$
HR3-RZT: $i = (1, 2, 4, 5, \ldots, 13, 14),\ j = (3, 6, \ldots, 15, 16)$.

Thus, Eqs. (16) represent a system of $N_{eq}$ simultaneous algebraic equations that are readily solved for the $N_{eq}$ unknowns $(F_0, U_0)$ by standard matrix inversion. In the present work, computations of all stiffness terms and shear correction factors, and the matrix inversion operations were carried out in MATLAB.

### *2.1.2. Model validation*

To test the general applicability of the HR models a variety of different symmetric and non-symmetric composite laminates and sandwich plates are tested. Table 1 shows the two different materials used throughout the analysis. The first material c is representative of a high-performance carbon-fibre reinforced plastic with high orthotropy of in-plane modulus to transverse shear modulus. The second material h is a transversely isotropic honeycomb core and features significantly lower transverse shear stiffness than material c to exacerbate the ZZ effect. The stacking sequences of different laminates including layer orientations, layer thicknesses and layer material codes are summarised in Table 2.

Laminates A and B are composite laminates, whereas laminates C and D are sandwich plates. Laminate D features two different kinds of sandwich core, the full constitutive core h and the degraded core 0.01h, where for the latter, all material moduli of material h are degraded by a factor of 100. As a variety of thin and thick laminates with characteristic length to thickness ratios ranging from $a/t = 100$ to $a/t = 5$ are investigated in this section, the layer thicknesses are quoted as ratios of the total laminate thickness.

Henceforth, all deflection and stress results are presented in normalised form. The chosen metrics for assessing the accuracy of the HR models are the maximum transverse bending deflection $w_0$ and the full 3D stress field, i.e. axial stress $\sigma_x$, lateral stress $\sigma_y$, in-plane shear stress $\sigma_{xy}$, transverse shear stresses $\tau_{xz}$ and $\tau_{yz}$, and transverse normal stress $\sigma_z$. The normalised quantities are defined as follows:

$$
\begin{aligned}
&\bar{w}_0 = \frac{E_2^{(c)} t^2}{p_0 a^2 b^2} \int_{-\frac{t}{2}}^{\frac{t}{2}} u_z \left(\frac{a}{2}, \frac{b}{2}, z\right) \mathrm{d}z, \\
&\bar{\sigma}_x(z) = \frac{t^2}{p_0 a^2} \sigma_x \left(\frac{a}{2}, \frac{b}{2}, z\right),\ \bar{\sigma}_y(z) = \frac{t^2}{p_0 b^2} \sigma_y \left(\frac{a}{2}, \frac{b}{2}, z\right), \\
&\bar{\sigma}_{xy}(z) = \frac{t^2}{p_0 a b} \sigma_{xy} \left(\frac{a}{4}, \frac{b}{4}, z\right),\ \bar{\sigma}_{xz}(z) = \frac{1}{p_0} \sigma_{xz} \left(0, \frac{b}{2}, z\right), \\
&\bar{\sigma}_{yz}(z) = \frac{1}{p_0} \sigma_{yz} \left(\frac{a}{2}, 0, z\right),\ \bar{\sigma}_z(z) = \frac{1}{p_0} \sigma_z \left(\frac{a}{2}, \frac{b}{2}, z\right)
\end{aligned}
\tag{17}
$$

and are calculated at the indicated locations $(x, y, z)$ throughout the 3D plate. Note that the bending deflection is normalised using the matrix-dominated modulus $E_2^{(c)}$ of material c. Furthermore, the normalised bending deflection $\bar{w}_0$ for the HR models is constant through the thickness of each laminate and is thus compared against Pagano's [35] normalised average through-thickness deflection. As $\bar{w}_0$ is calculated at the in-plane centroid of the plate, this metric corresponds to the maximum bending deflection. Similarly, the normal stress metrics $\bar{\sigma}_x$, $\bar{\sigma}_y$ and $\bar{\sigma}_z$ are also computed at the in-plane centroid of the plate. The two transverse shear stress metrics $\bar{\sigma}_{xz}$ and $\bar{\sigma}_{yz}$ are calculated at the midspan locations of the supported edges, whereas the in-plane shear stress is taken at the quarterspan of both in-plane $x$- and $y$-dimensions.

The relative percentage errors in the normalised metrics of Eq. (17) for the four HR models HR3, HR3-RZT, HR3-RZTmx and HR3-MZZF with respect to Pagano's 3D elasticity solution [35] are shown Tables 3-6. The results for Pagano's solution are given to four significant figures, whereas the percentage errors are cited to two decimal places. These tables allow the accuracy of the four HR models to be compared for a number of different stacking sequences and characteristic length to thickness ratios ranging from thin laminates with $a/t = 100$ to thick laminates with $a/t = 5$.

As indicated by the table headings, the results in Tables 3-6 compare the absolute maximum through-thickness values of the stress metrics $\bar{\sigma}_x$, $\bar{\sigma}_y$, $\bar{\sigma}_{xy}$, $\bar{\sigma}_{xz}$ and $\bar{\sigma}_{yz}$, where the notation $\vee|m|$ is used to indicate the absolute maximum value of metric $m$ through the thickness of the plate. For the transverse normal stress metric $\bar{\sigma}_z$, the value at the interface $z = z_{N_l - 1}$ between layers $N_l$ and $N_l - 1$, i.e. at the first layer interface from the top of the laminate, is used. Laminate A is a three-layer laminate and therefore the RZT modification rule for EWLs given in Eq. (11) need not be applied. As a result, the models HR3-RZT and HR3-RZTmx are the same and are combined under a single heading HR3-RZT in Table 3.

The results in Tables 3-4 show that the error in the HR3 model without ZZ functionality is around 1% for the non-sandwich laminates A and B with $a/t$ ratios up to 20. However, the HR3 model loses accuracy compared to the ZZ HR models when $a/t \leq 10$. For laminate A, the error in $\bar{\sigma}_x$ is as great as 4.25% for $a/t = 10$ and then increases to 8.05% for $a/t = 5$. However, as plies are blocked together into relatively thick groups in laminates A and B, part of the error in HR3 is due to the ZZ effect that arises from the difference in transverse shear moduli of the 0° and 90° layers. In practical engineering laminates, where plies are regularly dispersed to prevent transverse matrix cracking, the influence of ZZ effects diminishes. Thus, for general engineering laminates, the HR3 model can safely be considered to be applicable for composite, non-sandwich plates up to $a/t$ ratios of around 10. The increasing discrepancy for $a/t = 5$ is due to the increasing effects of normal through-

**Table 1:** Mechanical properties of materials c and h.

| **Material** | $E_1$ | $E_2$ | $E_3$ | $G_{12}$ | $G_{13}$ | $G_{23}$ |
|---|---|---|---|---|---|---|
| c | 172.5 GPa | 6.9 GPa | 6.9 GPa | 3.45 GPa | 3.45 GPa | 1.38 GPa |
| h | 276 MPa | 276 MPa | 3.45 GPa | 110.4 MPa | 414 MPa | 414 MPa |
| **Material** | $\nu_{12}$ | | $\nu_{13}$ | | $\nu_{23}$ | |
| c | 0.25 | | 0.25 | | 0.25 | |
| h | 0.25 | | 0.02 | | 0.02 | |

**Table 2:** Analysed orthotropic stacking sequences. Subscripts indicate the repetition of a property over the corresponding number of layers. Layer thicknesses stated as ratios of total laminate thickness.

| **Laminate** | **Thickness Ratio** | **Material** | **Stacking Sequence** |
|---|---|---|---|
| A | $[(1/3)_3]$ | $[c_3]$ | [0/90/0] |
| B | $[0.25_4]$ | $[c_4]$ | [0/90/0/90] |
| C | [0.1/0.3/0.35/0.25] | $[c_2/h/c]$ | [0/90/0/90] |
| D | $[0.1_2/0.3/0.4/0.05_2]$ | $[c_2/0.01h/h/c_2]$ | $[90/0_3/90/0]$ |

**Table 3:** Orthotropic laminate A: Percentage error in normalised bending deflection and 3D stresses for various HR models and $a/t$ ratios with respect to Pagano's solution [35].

| $a/t$ | **Model** | $\lvert\bar{w}_0\rvert$ | $\vee\lvert\bar{\sigma}_x\rvert$ | $\vee\lvert\bar{\sigma}_y\rvert$ | $\vee\lvert\bar{\sigma}_{xy}\rvert$ | $\vee\lvert\bar{\sigma}_{xz}\rvert$ | $\vee\lvert\bar{\sigma}_{yz}\rvert$ | $\bar{\sigma}_z(z_{N_l-1})$ |
|---|---|---|---|---|---|---|---|---|
| 100 | **Pagano** | **0.004347** | **0.5393** | **0.1808** | **0.01068** | **39.47** | **8.282** | **-0.7407** |
| | HR3 (%) | 0.01 | 0.05 | -0.02 | 0.03 | 0.01 | -0.01 | 0.00 |
| | HR3-RZT (%) | 0.01 | 0.00 | -0.02 | -0.01 | 0.00 | -0.01 | 0.00 |
| | HR3-MZZF (%) | 0.01 | 0.00 | -0.02 | 0.00 | 0.00 | -0.01 | 0.00 |
| 50 | **Pagano** | **0.004451** | **0.5410** | **0.1846** | **0.01082** | **19.67** | **4.212** | **-0.7406** |
| | HR3 (%) | 0.03 | 0.22 | -0.07 | 0.13 | 0.03 | -0.03 | 0.01 |
| | HR3-RZT (%) | 0.02 | 0.01 | -0.07 | 0.01 | 0.01 | -0.04 | 0.00 |
| | HR3-MZZF (%) | 0.03 | 0.01 | -0.07 | 0.01 | 0.01 | -0.04 | 0.00 |
| 20 | **Pagano** | **0.005162** | **0.5525** | **0.2101** | **0.01170** | **7.692** | **1.875** | **-0.7398** |
| | HR3 (%) | 0.15 | 1.28 | -0.39 | 0.76 | 0.17 | -0.16 | 0.04 |
| | HR3-RZT (%) | 0.14 | 0.09 | -0.27 | 0.40 | 0.04 | -0.19 | 0.00 |
| | HR3-MZZF (%) | 0.14 | 0.07 | -0.38 | 0.04 | 0.04 | -0.19 | 0.01 |
| 10 | **Pagano** | **0.007524** | **0.5906** | **0.2882** | **0.01449** | **3.573** | **1.228** | **-0.7371** |
| | HR3 (%) | 0.50 | 4.25 | -1.17 | 2.37 | 0.64 | -0.29 | 0.17 |
| | HR3-RZT (%) | 0.33 | 0.02 | -1.09 | 0.91 | 0.11 | -0.30 | 0.06 |
| | HR3-MZZF (%) | 0.42 | 0.08 | -1.17 | 0.19 | 0.15 | -0.44 | 0.05 |
| 5 | **Pagano** | **0.01528** | **0.7180** | **0.4784** | **0.02185** | **1.471** | **0.9557** | **-0.7264** |
| | HR3 (%) | 1.28 | 8.05 | -2.97 | 5.56 | -0.35 | 0.25 | 0.76 |
| | HR3-RZT (%) | 0.97 | -2.18 | -3.03 | 1.07 | 0.41 | -0.15 | 0.45 |
| | HR3-MZZF (%) | 0.97 | -2.20 | -3.05 | 1.03 | 0.39 | -0.15 | 0.44 |

**Table 4:** Orthotropic laminate B: Percentage error in normalised bending deflection and 3D stresses for various HR models and $a/t$ ratios with respect to Pagano's solution [35].

| $a/t$ | Model | $\lvert\bar{w}_0\rvert$ | $\vee\lvert\bar{\sigma}_x\rvert$ | $\vee\lvert\bar{\sigma}_y\rvert$ | $\vee\lvert\bar{\sigma}_{xy}\rvert$ | $\vee\lvert\bar{\sigma}_{xz}\rvert$ | $\vee\lvert\bar{\sigma}_{yz}\rvert$ | $\bar{\sigma}_z(z_{N_l-1})$ |
|---|---|---|---|---|---|---|---|---|
| | **Pagano** | **0.005169** | **0.4887** | **0.4886** | **0.01259** | **14.02** | **14.02** | **-0.8599** |
| | HR3 (%) | 0.03 | -0.01 | 0.01 | 0.08 | 0.03 | 0.04 | 0.00 |
| 50 | HR3-RZT (%) | 0.05 | 0.07 | 0.00 | 0.51 | -0.05 | -0.05 | -0.04 |
| | HR3-RZTmx (%) | 0.03 | -0.03 | -0.01 | 0.02 | 0.00 | 0.00 | 0.00 |
| | HR3-MZZF (%) | 0.03 | 0.03 | 0.04 | 0.08 | 0.00 | 0.00 | 0.00 |
| | **Pagano** | **0.005713** | **0.4982** | **0.4979** | **0.01305** | **5.567** | **5.567** | **-0.8590** |
| | HR3 (%) | 0.16 | -0.03 | 0.03 | 0.50 | 0.21 | 0.21 | 0.00 |
| 20 | HR3-RZT (%) | 0.15 | 0.19 | 0.25 | 0.50 | 0.02 | 0.02 | 0.00 |
| | HR3-RZTmx (%) | 0.15 | -0.15 | -0.09 | 0.12 | 0.01 | 0.01 | 0.00 |
| | HR3-MZZF (%) | 0.15 | 0.18 | 0.25 | 0.50 | 0.02 | 0.02 | 0.00 |
| | **Pagano** | **0.007617** | **0.5306** | **0.5309** | **0.01460** | **2.715** | **2.720** | **-0.8557** |
| | HR3 (%) | 0.57 | -0.02 | -0.07 | 1.80 | 0.90 | 0.72 | 0.01 |
| 10 | HR3-RZT (%) | 0.44 | 0.75 | 0.67 | 1.93 | 0.15 | -0.02 | 0.04 |
| | HR3-RZTmx (%) | 0.44 | -0.48 | -0.53 | 0.46 | 0.13 | -0.04 | 0.02 |
| | HR3-MZZF (%) | 0.44 | 0.74 | 0.69 | 1.75 | 0.15 | -0.02 | 0.03 |
| | **Pagano** | **0.01475** | **0.6384** | **0.6560** | **0.01985** | **1.245** | **1.264** | **-0.8430** |
| | HR3 (%) | 1.73 | 0.77 | -1.94 | 5.02 | 3.16 | 1.55 | 0.21 |
| 5 | HR3-RZT (%) | 0.87 | 2.64 | -0.28 | 4.98 | 0.81 | -0.72 | 0.31 |
| | HR3-RZTmx (%) | 0.86 | -0.95 | -3.61 | 1.54 | 1.03 | -0.54 | 0.25 |
| | HR3-MZZF (%) | 0.86 | 2.56 | -0.20 | 4.73 | 0.83 | -0.74 | 0.31 |

**Table 5:** Orthotropic laminate C: Percentage error in normalised bending deflection and 3D stresses for various HR models and $a/t$ ratios with respect to Pagano's solution [35].

| $a/t$ | Model | $\lvert\bar{w}_0\rvert$ | $\vee\lvert\bar{\sigma}_x\rvert$ | $\vee\lvert\bar{\sigma}_y\rvert$ | $\vee\lvert\bar{\sigma}_{xy}\rvert$ | $\vee\lvert\bar{\sigma}_{xz}\rvert$ | $\vee\lvert\bar{\sigma}_{yz}\rvert$ | $\bar{\sigma}_z(z_{N_l-1})$ |
|---|---|---|---|---|---|---|---|---|
| | **Pagano** | **0.006048** | **0.2451** | **0.6576** | **0.01883** | **3.268** | **19.69** | **-0.8002** |
| | HR3 (%) | 0.03 | 0.07 | 0.46 | 0.08 | -0.15 | 0.08 | 0.01 |
| 50 | HR3-RZT (%) | 0.03 | -0.07 | 0.03 | 0.04 | -0.08 | 0.01 | 0.00 |
| | HR3-RZTmx (%) | 0.03 | -0.06 | 0.01 | 0.04 | -0.08 | 0.01 | 0.00 |
| | HR3-MZZF (%) | 0.03 | -0.04 | 0.19 | 0.16 | -0.10 | 0.02 | 0.00 |
| | **Pagano** | **0.008037** | **0.3159** | **0.6757** | **0.02216** | **1.605** | **7.357** | **-0.7997** |
| | HR3 (%) | 0.24 | 0.54 | 2.64 | 0.50 | -0.62 | 0.47 | 0.08 |
| 20 | HR3-RZT (%) | 0.15 | -0.30 | 0.16 | 0.21 | -0.38 | 0.09 | -0.01 |
| | HR3-RZTmx (%) | 0.15 | -0.30 | 0.04 | 0.21 | -0.39 | 0.09 | -0.01 |
| | HR3-MZZF (%) | 0.16 | -0.16 | 1.06 | 0.84 | -0.40 | 0.14 | 0.01 |
| | **Pagano** | **0.01384** | **0.4927** | **0.7746** | **0.03001** | **1.154** | **3.193** | **-0.7970** |
| | HR3 (%) | 1.02 | 2.31 | 10.82 | 1.82 | -0.87 | -2.97 | 0.26 |
| 10 | HR3-RZT (%) | 0.44 | -0.68 | 0.91 | 0.72 | -0.80 | 0.20 | -0.02 |
| | HR3-RZTmx (%) | 0.44 | -0.67 | 0.17 | 0.72 | -0.81 | 0.26 | -0.03 |
| | HR3-MZZF (%) | 0.52 | -0.12 | 6.97 | 2.46 | -0.64 | -0.77 | 0.02 |
| | **Pagano** | **0.02969** | **0.8067** | **1.081** | **0.04158** | **0.8103** | **1.649** | **-0.7829** |
| | HR3 (%) | 2.74 | 7.49 | 21.13 | 5.28 | -0.08 | -6.96 | 0.81 |
| 5 | HR3-RZT (%) | 0.95 | -1.03 | 1.64 | 1.96 | -0.95 | 1.54 | 0.10 |
| | HR3-RZTmx (%) | 0.95 | -1.02 | 0.32 | 1.95 | -0.96 | 1.56 | 0.10 |
| | HR3-MZZF (%) | 1.23 | 0.79 | 12.57 | 6.08 | -0.20 | 0.35 | 0.22 |

**Table 6:** Orthotropic laminate D: Percentage error in normalised bending deflection and 3D stresses for various HR models and $a/t$ ratios with respect to Pagano's solution [35].

| $a/t$ | Model | $\lvert\bar{w}_0\rvert$ | $\vee\lvert\bar{\sigma}_x\rvert$ | $\vee\lvert\bar{\sigma}_y\rvert$ | $\vee\lvert\bar{\sigma}_{xy}\rvert$ | $\vee\lvert\bar{\sigma}_{xz}\rvert$ | $\vee\lvert\bar{\sigma}_{yz}\rvert$ | $\bar{\sigma}_z(z_{N_l-1})$ |
|---|---|---|---|---|---|---|---|---|
| | **Pagano** | **0.02123** | **1.153** | **1.190** | **0.02576** | **9.003** | **9.478** | **-0.9849** |
| | HR3 (%) | 0.25 | 6.07 | 3.64 | 16.16 | -0.50 | -0.41 | -0.05 |
| 50 | HR3-RZT (%) | 0.00 | 0.01 | 0.02 | 0.00 | 0.00 | 0.00 | 0.00 |
| | HR3-RZTmx (%) | 0.00 | 0.00 | 0.01 | 0.01 | 0.00 | 0.00 | 0.00 |
| | HR3-MZZF (%) | 0.23 | 7.24 | 0.69 | 21.83 | -0.52 | -0.37 | -0.06 |
| | **Pagano** | **0.08638** | **1.599** | **1.643** | **0.05179** | **4.072** | **4.285** | **-0.9817** |
| | HR3 (%) | 2.02 | 25.88 | 11.18 | 28.06 | -8.98 | -2.42 | -0.27 |
| 20 | HR3-RZT (%) | 0.00 | 0.01 | 0.04 | 0.05 | 0.03 | 0.01 | 0.00 |
| | HR3-RZTmx (%) | 0.00 | -0.02 | 0.03 | 0.06 | 0.01 | 0.01 | 0.00 |
| | HR3-MZZF (%) | 1.79 | 30.62 | 9.49 | 44.21 | -5.93 | -3.73 | -0.34 |
| | **Pagano** | **0.2483** | **3.169** | **3.668** | **0.1281** | **3.723** | **3.792** | **-0.9738** |
| | HR3 (%) | 6.71 | 29.18 | 20.13 | 26.56 | -10.86 | 3.32 | -0.91 |
| 10 | HR3-RZT (%) | -0.06 | 0.51 | 0.43 | 0.45 | 0.46 | 0.42 | 0.01 |
| | HR3-RZTmx (%) | -0.06 | 0.42 | 0.42 | 0.48 | 0.42 | 0.42 | 0.01 |
| | HR3-MZZF (%) | 5.90 | 36.23 | 17.20 | 46.60 | -5.84 | -1.31 | -1.14 |
| | **Pagano** | **0.5129** | **6.188** | **6.565** | **0.2376** | **3.131** | **3.148** | **-0.9600** |
| | HR3 (%) | 13.38 | 24.97 | 35.38 | 38.74 | -1.89 | 16.38 | -2.07 |
| 5 | HR3-RZT (%) | -1.12 | 4.19 | 4.38 | 4.37 | 4.42 | 4.46 | 0.18 |
| | HR3-RZTmx (%) | -1.12 | 4.15 | 4.37 | 4.52 | 4.37 | 4.47 | 0.18 |
| | HR3-MZZF (%) | 11.50 | 31.84 | 30.70 | 61.03 | 3.37 | 9.34 | -2.52 |

thickness deformation. Thus, under these circumstances the HR formulation needs to be modified to account for thickness stretch.

For sandwich plates C and D (Tables 5 and 6), the accuracy of the HR3 model is inferior to the HR models with ZZ functionality. Without the ZZ degree of freedom, the HR3 model cannot account for the fact that layerwise differences in transverse shear moduli lead to changes in the $z$-wise slopes of the displacement and stress fields at layer interfaces. The pronounced transverse orthotropy between the composite layers c and the honeycomb layers h increases the ZZ effect in the sandwich plates C and D compared to composite laminates A and B. The errors in the HR3 model are especially pronounced for laminate D, which features both the honeycomb core h and the degraded core 0.01h. For this laminate the error in the in-plane shear stress metric $\bar{\sigma}_{xy}$ is around 16% for the relatively thin $a/t$ ratio of 50. For thicker laminates with $a/t = 10$ this error increases to over 25%. However, for sandwich plate C (Table 5), which only includes core h, the HR3 model maintains reasonable accuracy.

The HR3-RZT and HR3-RZTmx models are the most accurate of the HR formulations investigated herein, with a maximum error of 1.93% (Laminate B) for $a/t$ ratios up to 10. When the thickness of the plate is further increased to $a/t = 5$ the HR-RZT models are accurate to within 5% (Laminate D). As previously noted, the increasing inaccuracy for $a/t = 5$ arises because the effects of through-thickness normal deformation can no longer be ignored. However, given the highly orthotropic material properties and "cube"-like nature of a plate with $a/t = 5$, errors to within a few percent of a 3D elasticity solution are acceptable given the reduced computational effort of the HR model compared to the alternative of full 3D FEM analyses. Interestingly, for sandwich plate C both the HR3-RZT and HR3-RZTmx models are accurate to within 2% for the thick configuration $a/t = 5$. One possible explanation for this behaviour is that the low transverse shear rigidity of the sandwich core (414 MPa) with respect to the transverse normal modulus (3.45 GPa) makes it energetically favourable for the plate to deform via transverse shearing and ZZ mechanisms rather than by transverse normal deformation, thereby reducing the relative influence of inaccuracies associated with neglecting thickness stretch.

Based on these findings, the difference in accuracy between the HR3-RZT and HR3-RZTmx models is benign. Gherlone [33] modified the definition of the RZT ZZ function based on observations of the in-plane displacement fields, but the present results suggest that the effect of EWLs is less pronounced for stress fields. Stresses are based on the derivatives of displacements, and therefore differences in the displacements of the HR3-RZT and HR3-RZTmx models do not necessarily mean the stresses are different. However, given that accurate internal displacement fields are needed in many nonlinear failure analyses, such as cohesive zone models, Gherlone's [33] modified version of the RZT ZZ function is recommended for most accurate results.

The other third-order ZZ model based on MZZF, HR3-MZZF, shows similar accuracy to the HR models based

on the RZT ZZ function for composite laminates A-B and sandwich plate C. For composite laminates A-B, all seven metrics are accurate to within 2% for $a/t$ ratios up to 10. When the thickness of the plate is further increased to $a/t = 5$, the HR3-MZZF model also suffers from a loss in accuracy to around 5% due to the thickness stretch effect. The first discrepancy between the accuracy of the RZT- and MZZF-based HR models can be observed for sandwich plate C. For this plate, the error in $\bar{\sigma}_y$ of the HR3-MZZF model is close to 7% when $a/t = 10$, whereas the HR3-RZTmx model remains within 2% even for the thicker configuration of $a/t = 5$.

For sandwich plate D, which comprises two different core materials h and 0.01h, the errors in HR3-MZZF are more pronounced and are in fact comparable to the accuracy of the HR3 model without ZZ functionality. The error in $\bar{\sigma}_{xy}$ is around 22% for the relatively thin configuration of $a/t = 50$ and increases to 47% for the moderately thick configuration at $a/t = 10$. In comparison, the error in the RZT-based HR models is less than 1% for sandwich plate D up to $t/a = 10$.

These observations corroborate the findings of previous work [33, 36] that MZZF loses accuracy for laminates comprising three different constitutive materials. This is because MZZF does not formally account for differences in the transverse shear moduli that underlie the mechanics of the ZZ effect. It is perhaps appropriate to point out the caveat in the original paper by Toledano and Murakami [37] that the "inclusion of the zig-zag shaped $C^0$ function was motivated by the displacement microstructure of *periodic* laminated composites" and that "for general laminate configurations, this periodicity is destroyed", such that the "theory should be expected to break down in these particular cases".

However, the authors would like to emphasise that, in general, MZZF provides accurate solutions for most commonly used laminates when employed in a third-order HR theory. For sandwich plates with very flexible cores or laminates with pronounced heterogeneity, the constitutive independence of MZZF can lead to large errors. Thus, the RZT ZZ function should be used for the most general straight-fibre laminations.

To qualitatively compare the accuracy of the four HR models, the through-thickness variations of all six stress metrics are plotted in Figures 3-14 for the characteristic length to thickness ratio $a/t = 10$. The in-plane $(x, y)$ locations of each $z$-wise plot are provided in the stress metric definitions of Eq. (17) and are additionally indicated in the figure captions. The observations previously made about the data in Tables 3-6 are corroborated in these figures, namely:

1. The HR3-RZT and HR3-RZTmx through-thickness plots of the 3D stress fields closely match Pagano's 3D elasticity solution for any type of stacking sequence investigated herein. Most importantly, the transverse stress profiles are captured accurately from the *a priori* model assumptions, precluding the need for stress recovery steps.
2. The difference in the 3D stress fields between HR3-RZT and HR3-RZTmx models is benign.
3. The HR3 model generally only provides accurate 3D stress fields to within nominal errors for composite laminates. In the case of sandwich plates or laminates that feature materials with transverse shear properties that vary by orders of magnitude, a ZZ term is generally recommended. However for practical engineering laminates most commonly used in industry, the HR3 model provides the best trade-off between accuracy and computational effort.
4. A third-order model with a ZZ term based on MZZF is accurate for most composite laminates and stiff sandwich cores. In the case of more flexible or degraded sandwich cores, laminates with two different types of cores, or laminates with more than two unique constitutive materials, the HR3-MZZF model leads to large errors.
5. For characteristic length to thickness ratios $a/t \leq 5$, thickness stretch should be incorporated for generally accurate 3D stress fields. Thus, the assumed displacement field for $u_z$ needs to be modified to account for a higher-order variation through the thickness.

Note that the discrepancies between the two HR models HR3 and HR3-MZZF, and Pagano's 3D elasticity solution are most evident for sandwich laminate D comprising two different sandwich cores (see Figures 12-14).

An interesting phenomenon is observed in the transverse shear stress profiles of laminate D in Figures 14a and 14b. In these plots, a reversal of the transverse shear stresses in the stiffer face layers is observed. This behaviour only occurs for extreme cases of transverse orthotropy, i.e. when the transverse shear rigidity of an inner layer is insufficient to support the peak transverse shear stress of the adjacent outer layer. In essence, it is a load redistribution effect that arises because the transverse shear force must remain constant for a unique loading configuration, i.e. the transverse shear stress through-thickness distribution may change with layup, but the through-thickness integral of this transverse shear stress is independent of layup.

As the transverse shear stresses and in-plane stresses must equilibrate in Cauchy's equilibrium equations, we can also observe that the corresponding plots of $\bar{\sigma}_x$, $\bar{\sigma}_y$ and $\bar{\sigma}_{xy}$ for sandwich plate D change sign in some layers remote from the neutral axis. As a result, some of the layers are both in tension and compression even when they are situated far away from the neutral axis. Fundamentally, this means that a cross-section of the plate no longer has one unique neutral axis. The extreme case of transverse orthotropy occurs when the stiffer outer layers are bending independently with fully reversed in-plane stress profiles within one layer, i.e. equal amounts of tension and compression. Such a scenario occurs if the properties of the sandwich core are negligible, such that they have "air-like"

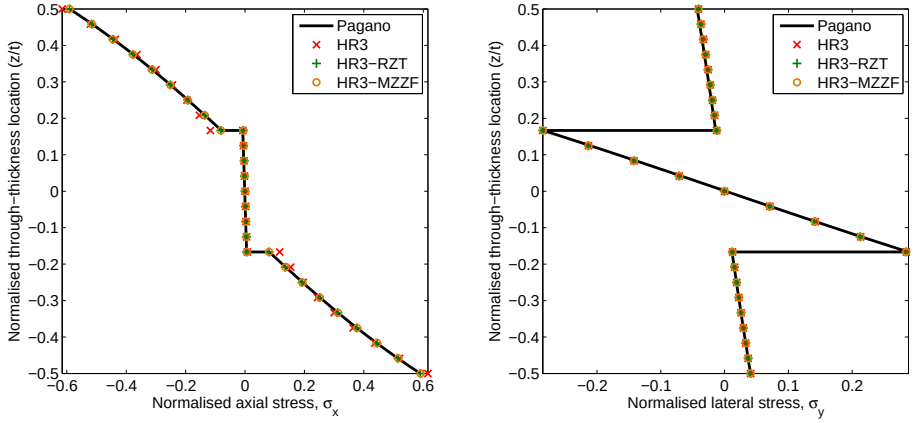


**(a)** Normalised axial stress, $\bar{\sigma}_x$ **(b)** Normalised lateral stress, $\bar{\sigma}_y$

**Figure 3:** Laminate A: Through-thickness distributions of the normalised axial ($\bar{\sigma}_x$) and lateral ($\bar{\sigma}_y$) stresses at $(a/2, b/2, z)$ for $a/t = 10$.

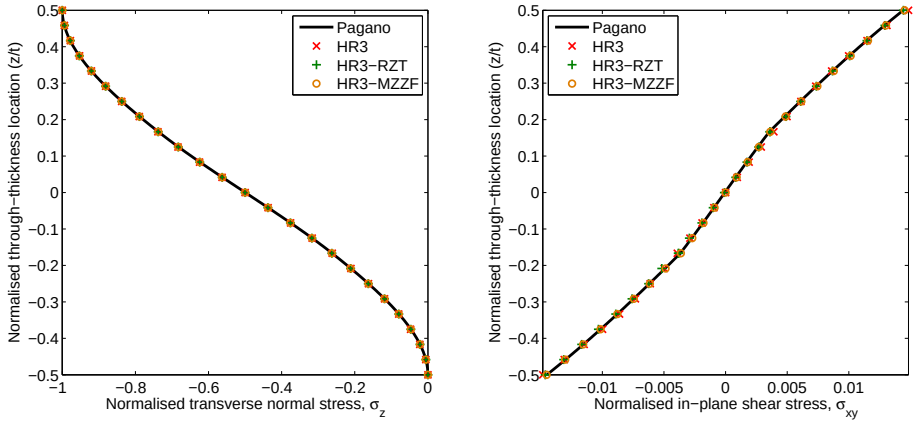


**(a)** Normalised transverse normal stress, $\bar{\sigma}_z$ **(b)** Normalised in-plane shear stress, $\bar{\sigma}_{xy}$

**Figure 4:** Laminate A: Through-thickness distributions of the normalised transverse normal ($\bar{\sigma}_z$) and in-plane shear ($\bar{\sigma}_{xy}$) stresses at $(a/2, b/2, z)$ and $(a/4, b/4, z)$, respectively for $a/t = 10$.

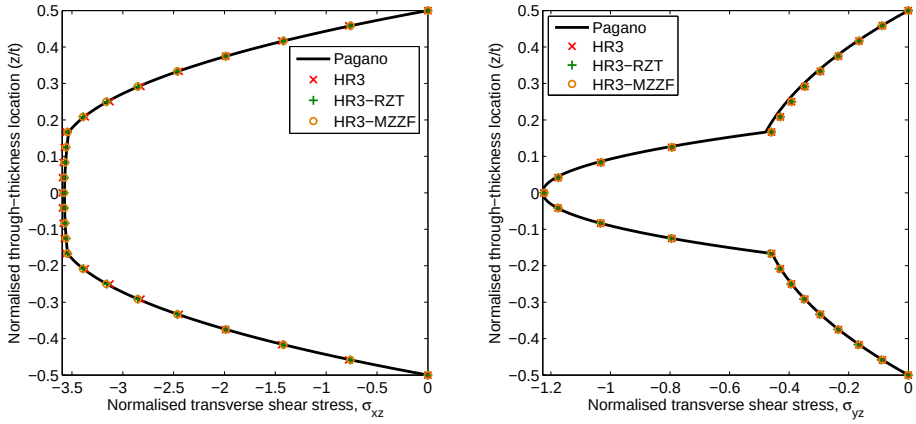


**(a)** Normalised transverse shear stress, $\bar{\sigma}_{xz}$ **(b)** Normalised transverse shear stress, $\bar{\sigma}_{yz}$

**Figure 5:** Laminate A: Through-thickness distributions of the normalised transverse shear stresses ($\bar{\sigma}_{xz}$ and $\bar{\sigma}_{yz}$) at $(0, b/2, z)$ and $(a/2, 0, z)$, respectively for $a/t = 10$.

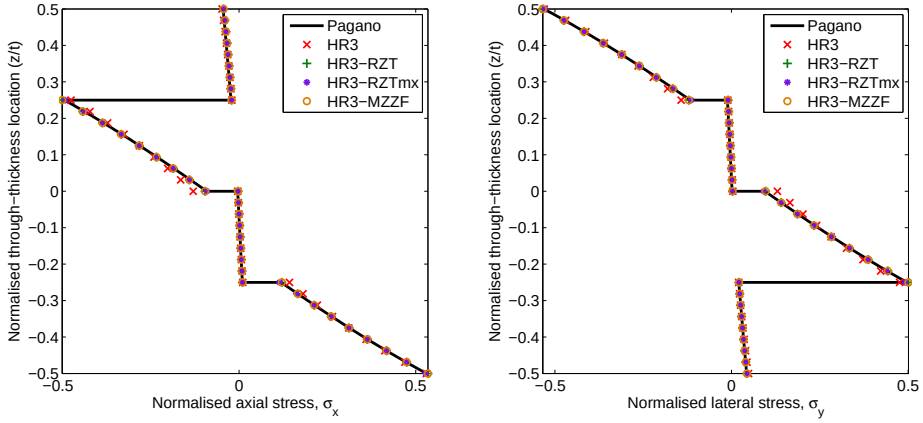


**(a)** Normalised axial stress, $\bar{\sigma}_x$ **(b)** Normalised lateral stress, $\bar{\sigma}_y$

**Figure 6:** Laminate B: Through-thickness distributions of the normalised axial ($\bar{\sigma}_x$) and lateral ($\bar{\sigma}_y$) stresses at $(a/2, b/2, z)$ for $a/t = 10$.

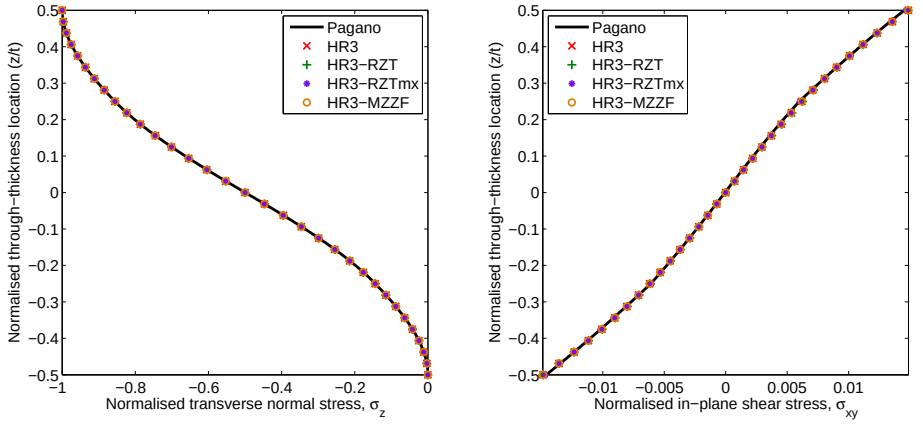


**(a)** Normalised transverse normal stress, $\bar{\sigma}_z$ **(b)** Normalised in-plane shear stress, $\bar{\sigma}_{xy}$

**Figure 7:** Laminate B: Through-thickness distributions of the normalised transverse normal ($\bar{\sigma}_z$) and in-plane shear ($\bar{\sigma}_{xy}$) stresses at $(a/2, b/2, z)$ and $(a/4, b/4, z)$, respectively for $a/t = 10$.

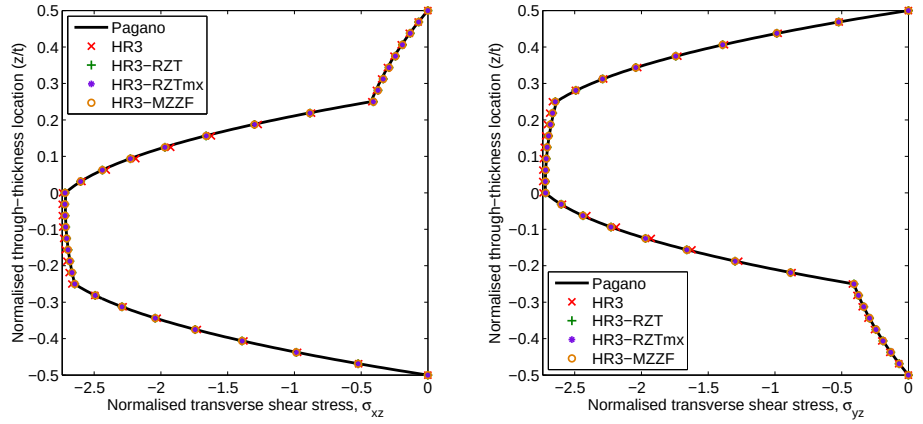


**(a)** Normalised transverse shear stress, $\bar{\sigma}_{xz}$ **(b)** Normalised transverse shear stress, $\bar{\sigma}_{yz}$

**Figure 8:** Laminate B: Through-thickness distributions of the normalised transverse shear stresses ($\bar{\sigma}_{xz}$ and $\bar{\sigma}_{yz}$) at $(0, b/2, z)$ and $(a/2, 0, z)$, respectively for $a/t = 10$.

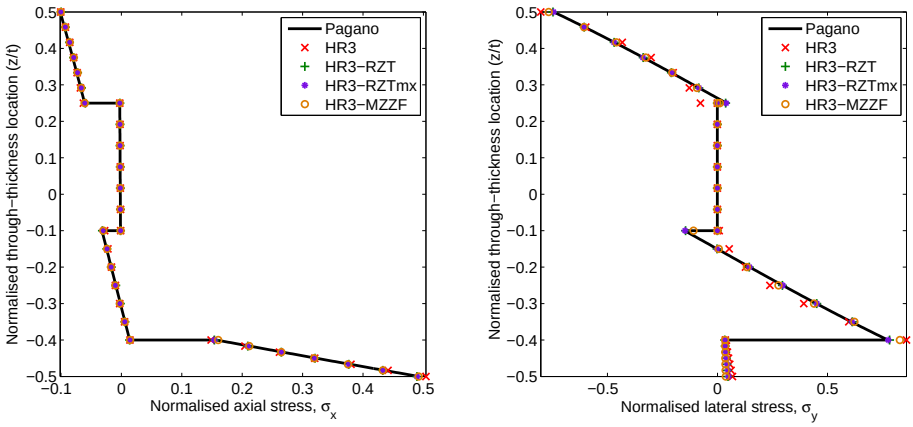


**(a)** Normalised axial stress, $\bar{\sigma}_x$ **(b)** Normalised lateral stress, $\bar{\sigma}_y$

**Figure 9:** Laminate C: Through-thickness distributions of the normalised axial ($\bar{\sigma}_x$) and lateral ($\bar{\sigma}_y$) stresses at $(a/2, b/2, z)$ for $a/t = 10$.

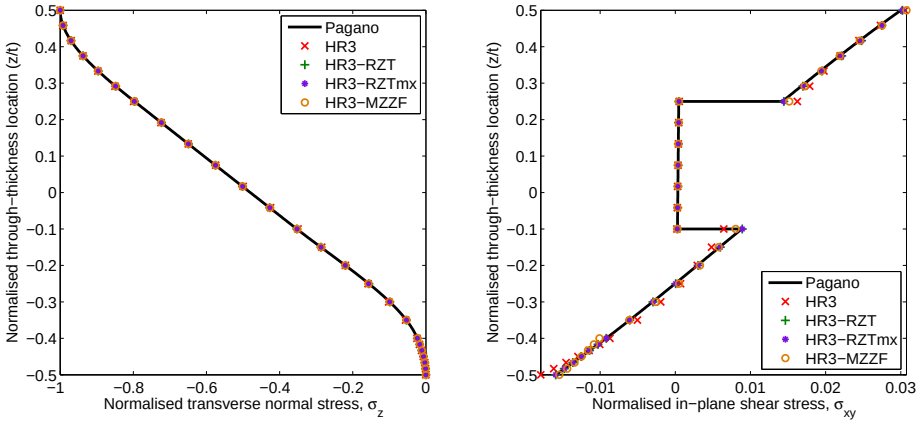


**(a)** Normalised transverse normal stress, $\bar{\sigma}_z$ **(b)** Normalised in-plane shear stress, $\bar{\sigma}_{xy}$

**Figure 10:** Laminate C: Through-thickness distributions of the normalised transverse normal ($\bar{\sigma}_z$) and in-plane shear ($\bar{\sigma}_{xy}$) stresses at $(a/2, b/2, z)$ and $(a/4, b/4, z)$, respectively for $a/t = 10$.

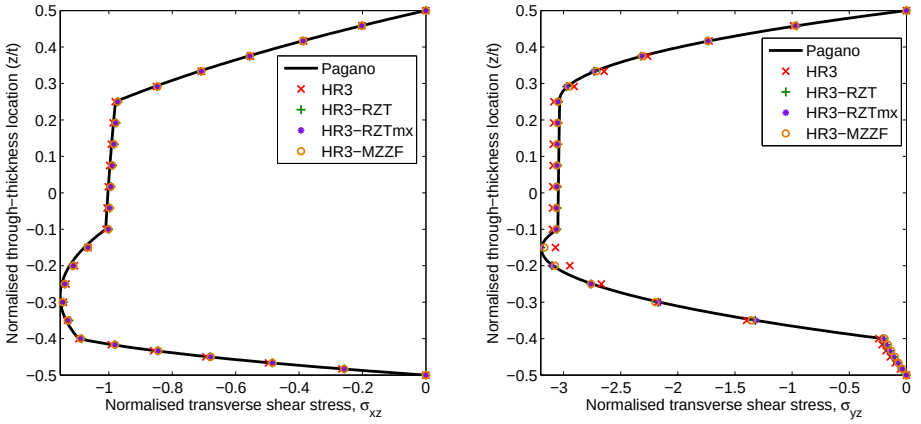


**(a)** Normalised transverse shear stress, $\bar{\sigma}_{xz}$ **(b)** Normalised transverse shear stress, $\bar{\sigma}_{yz}$

**Figure 11:** Laminate C: Through-thickness distributions of the normalised transverse shear stresses ($\bar{\sigma}_{xz}$ and $\bar{\sigma}_{yz}$) at $(0, b/2, z)$ and $(a/2, 0, z)$, respectively for $a/t = 10$.

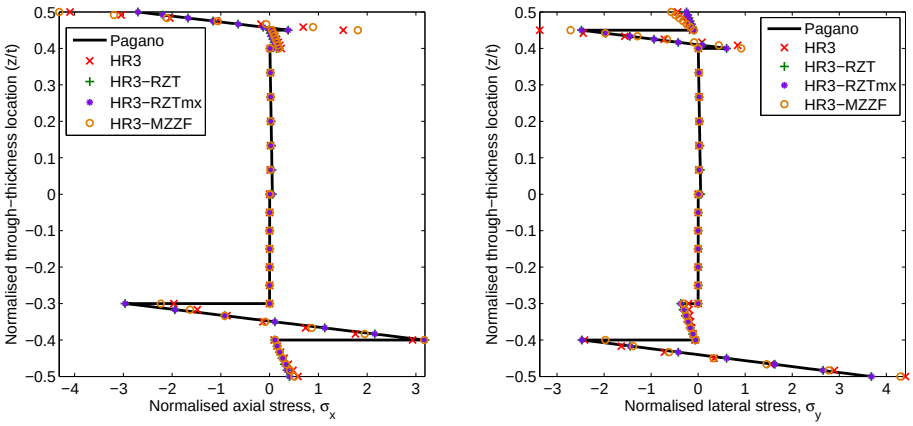


**(a)** Normalised axial stress, $\bar{\sigma}_x$ **(b)** Normalised lateral stress, $\bar{\sigma}_y$

**Figure 12:** Laminate D: Through-thickness distributions of the normalised axial ($\bar{\sigma}_x$) and lateral ($\bar{\sigma}_y$) stresses at $(a/2, b/2, z)$ for $a/t = 10$.

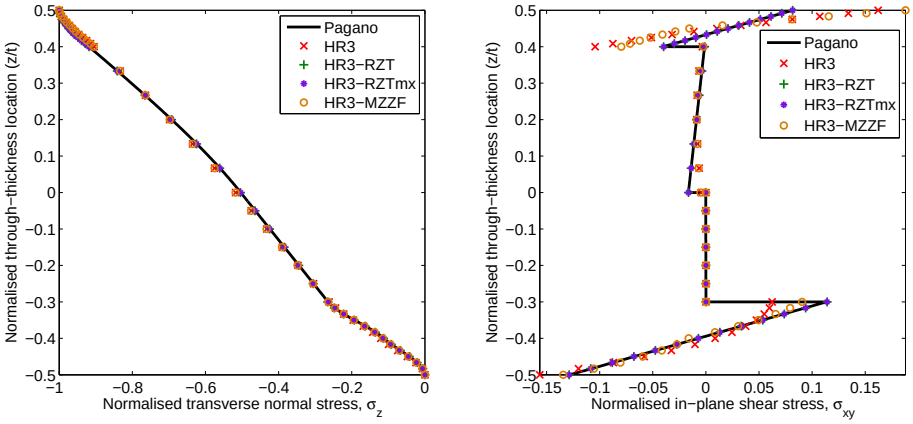


**(a)** Normalised transverse normal stress, $\bar{\sigma}_z$ **(b)** Normalised in-plane shear stress, $\bar{\sigma}_{xy}$

**Figure 13:** Laminate D: Through-thickness distributions of the normalised transverse normal ($\bar{\sigma}_z$) and in-plane shear ($\bar{\sigma}_{xy}$) stresses at $(a/2, b/2, z)$ and $(a/4, b/4, z)$, respectively for $a/t = 10$.

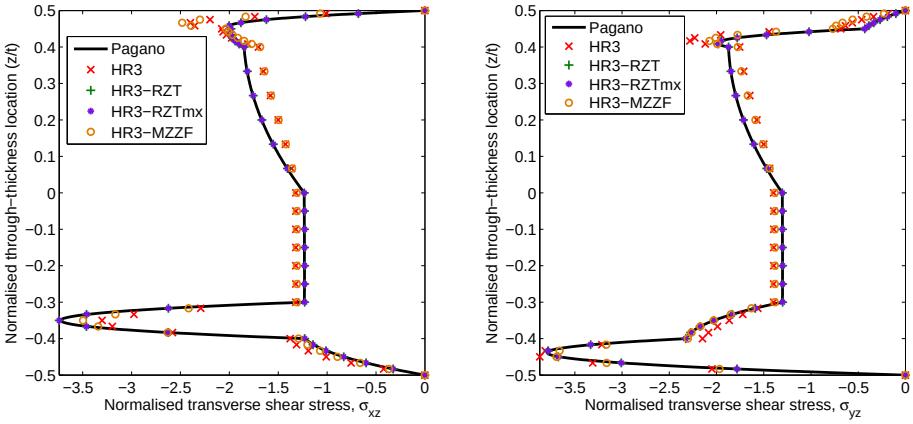


**(a)** Normalised transverse shear stress, $\bar{\sigma}_{xz}$ **(b)** Normalised transverse shear stress, $\bar{\sigma}_{yz}$

**Figure 14:** Laminate D: Through-thickness distributions of the normalised transverse shear stresses ($\bar{\sigma}_{xz}$ and $\bar{\sigma}_{yz}$) at $(0, b/2, z)$ and $(a/2, 0, z)$, respectively for $a/t = 10$.

properties that cannot support any shear loading.

In conclusion, the results for the orthotropic plates presented in this section corroborate the findings for orthotropic beams in [36]. The third-order RZT-based model is the most accurate of the formulations investigated herein for predicting bending deflections and 3D stress fields from *a priori* model assumptions. This is because the RZT ZZ function is derived from actual transverse shear material properties. The HR3-MZZF model provides similar accuracy for composite laminates and sandwich plates with benign transverse anisotropy between the core and face layers. For more pronounced anisotropy, the constitutive independence of MZZF can lead to large errors such that the HR3-RZTmx model is deemed to provide the most accurate 3D stress predictions for arbitrary straight-fibre laminations.

### *2.2. Benchmarking of 3D stresses in anisotropic laminates*

#### *2.2.1. Model implementation*

As a second test, consider the multilayered square plate ($a = b = 1$ m) shown in Figure 15, loaded on the top surface by a uniformly distributed pressure load $\hat{P}_t = p_0$ and a uniform shear traction in the $x$-direction $\hat{T}_{tx} = t_0$. The plate is rigidly built-in along all four edges, such that the three translations and three rotations are constrained through the entire cross-section. In the HR model, the 3D continuum is compressed onto an equivalent single layer $\Omega$ coincident with the midplane of the plate, depicted by the grey surface. This loading configuration represents a more challenging test case than the orthotropic plate subjected to sinusoidal pressure loading in the previous section, as both the layer fibre orientations and the loading condition are more general.

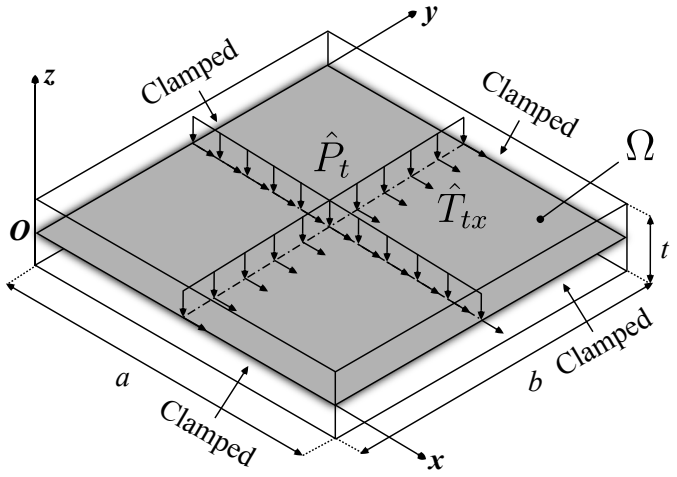


**Figure 15:** A composite plate loaded on the top surface by a uniformly distributed pressure load and a uniform shear traction. All four edges are clamped. In the HR model, the 3D continuum is compressed onto an equivalent single layer $\Omega$ coincident with the midplane of the plate.

For the anisotropic laminates investigated herein, the third-order model HR3, and third-order ZZ models HR3-RZT, HR3-RZTmx and HR3-MZZF are again implemented. As general anisotropic laminates with off-axis plies exhibit extension/shear and bend/twist coupling, it is more challenging to ascertain an analytical solution for the bending behaviour than for the orthotropic laminates in Section 2.1.2. For general anisotropic laminates $\bar{Q}_{16} \neq 0$ and $\bar{Q}_{26} \neq 0$, such that the simple double sine series solution previously implemented no longer exactly satisfies the governing differential equations.

The general governing equations are therefore solved using the pseudo-spectral differential quadrature method (DQM). Differential quadrature is a numerical discretisation technique proposed by Bellman et al. [38], that approximates the partial derivative of a functional field with respect to a specific spatial variable using a linear weighted sum of all the functional values in the domain. For example, the $n^{th}$ partial derivative of function $f(x)$ at the $i^{th}$ discretisation point is

$$\frac{\partial^n f(x_i)}{\partial x^n} = A_{ij}^{(n)} f(x_j) \quad i = 1, 2, \ldots, N_p \tag{18}$$

where $x_i$ is the set of $N_p$ discretisation points in the $x$-direction, typically defined by the non-uniform Gauss-Lobatto-Chebychev distribution, $A_{ij}^{(n)}$ are the weighting coefficients of the $n^{th}$ derivative, and repeated index $j$ means summation from 1 to $N_p$. The same technique is easily extended to the other two spatial dimensions to compute mixed derivatives.

The computations of the weighting coefficients are based on the generalised differential quadrature by Shu and Richard [39, 40], such that the the interpolating polynomials are based on Lagrange polynomial basis. In this manner, the interpolation coefficient matrix $g_k$ for a Lagrangian polynomial basis [41] is given by

$$g_k(x) = \frac{m(x)}{(x - x_k)m^{(1)}(x_k)}, \quad k = 1, 2, \ldots, N_p$$
$$m(x) = \prod_{j=1}^{N_p}(x - x_j), \; m^{(1)}(x_i) = \prod_{k=1, k\neq i}^{N_p}(x_i - x_k)$$

and this leads to the weighting coefficients of the derivatives $A_{ij}^{(n)}$,

$$A_{ij}^{(1)} = \frac{1}{x_j - x_i} \prod_{k=1, k\neq i,j}^{N_p} \frac{x_i - x_k}{x_j - x_k} \quad \text{for} \quad i \neq j$$
$$A_{ii}^{(1)} = \sum_{k=1, k\neq i}^{N_p} \frac{1}{x_i - x_k}. \tag{19}$$

Subsequently, all higher order weighting coefficients are obtained by direct matrix multiplication, i.e. $[A^{(m)}] = [A^{(1)}][A^{(n-1)}]$, with $n = 2, 3, \ldots, N_p - 1$ [42]. In this man-

ner, any set of linear differential equations can be expressed as a linear system of algebraic equations by replacing the differential operators with the weighting matrix in Eq. (19). Thus, the unknown functional values $f(x_i)$ at each grid point are found by solving the system of equations with the appropriate boundary conditions. The DQM is a versatile numerical discretisation technique that can be used to develop strong-form finite elements [43]. Using this technique, the relatively simple geometry of a square, flat plate investigated here can be extended to the analysis of more complex geometries.

The advantage of the DQM is that the differential-algebraic relation of Eq. (18) allows differential equations to be solved in the strong form, i.e. the differential relations are solved exactly for each grid point, rather than in an average sense over the whole domain, as is the case in the classic weak-form FEM based on the generalised Galerkin method of weighted residuals. This means that both essential and natural boundary conditions are enforced along the boundary points such that local stress gradients towards boundaries are captured with relatively few degrees of freedom. In the weak-form FEM, the natural boundary conditions are not enforced explicitly but the solution generally converges to satisfy the natural boundary condition with increasing mesh density.

Following the description of DQM, the governing differential equations are converted into algebraic ones by replacing the differential operators in the governing field equations (4) and boundary conditions (5) with DQ weighting matrices that operate on all functional unknowns within the domain. Thus, each differential operator is converted into a linear weighted sum of the functional unknowns at predetermined grid points. In this work, the non-uniform Chebychev-Gauss-Lobatto grid is used to discretise the planar domain of the continuum $x \in [0,1]$ and $y \in [0,1]$ into a computational domain with $N_p$ grid points in either direction. In the Chebychev-Gauss-Lobatto grid, the location of the grid points $X_i$ in direction $X$ is given by

$$X_i = \frac{1}{2}\left(1 - \cos\frac{(i-1)\,\pi}{N_p - 1}\right) \quad \text{for} \quad i = 1, 2, \ldots, N_p. \tag{20}$$

An important characteristic of the Chebychev-Gauss-Lobatto grid is that it results in the minimum discretisation error, and by biasing the grid points towards the boundaries, avoids Runge's phenomenon[1] associated with a uniform grid [42]. Based on an initial mesh convergence study, a disretisation grid with 19 points in both the $x$- and $y$- directions was chosen (see Figure 16). The chosen mesh size of 361 grid points provides a good trade-off between computational time and accuracy of the results.

Following the generalised approach by Shu and Du [44], the governing field equations (4) are discretised only for the internal grid points, whereas the boundary conditions (5) are only applied on the boundary points. Both sets of equations are expressed in terms of two unknown vectors: a vector of internal field unknowns $\mathcal{U}_i$ and a vector of boundary unknowns $\mathcal{U}_b$. This step of splitting the problem into internal and boundary points, as well as into field and boundary equations, is depicted in Figure 16. In this manner, the complete set of governing equations is substructured into four unique matrices that allow the boundary unknowns to be eliminated,

$$\mathcal{U}_i = \left[\boldsymbol{K_{ii}} - \boldsymbol{K_{ib}}\boldsymbol{K_{bb}}^{-1}\boldsymbol{K_{bi}}\right]^{-1} \cdot \left(F_i - \boldsymbol{K_{ib}}\boldsymbol{K_{bb}}^{-1} \cdot F_b\right) \tag{21a}$$

$$\mathcal{U}_b = \boldsymbol{K_{bb}}^{-1} \cdot \left(F_b - \boldsymbol{K_{bi}} \cdot \mathcal{U}_i\right) \tag{21b}$$

where $i$ refers to the internal field and $b$ to the boundary. Thus, the final matrix inversion problem in Eq. (21a) includes both the discretised field and boundary equations in one matrix, which is solved for the vector of internal field unknowns $\mathcal{U}_i$. The unknowns on the boundary $\mathcal{U}_b$ are subsequently post-processed using the internal field variables in Eq. (21b).

It is important to point out that the stiffness matrices in Eq. (21) are densely populated, such that certain preconditioning steps are recommended to reduce the condition number[2] of the associated matrices and to improve the accuracy of the matrix inversion. For variable-stiffness laminates, the material properties change across the discretisation grid such that the magnitudes of the terms along the rows of the stiffness matrices may vary significantly. Moreover, in the governing field equations and boundary conditions Eqs. (4)-(5), the unknown stress resultants $\mathcal{F}$ and their in-plane derivatives are multiplied by compliance terms $\boldsymbol{s}$ and shear correction factors $\boldsymbol{\eta}$. These material property-dependent terms can be orders of magnitude smaller than the DQM weighting coefficients which appear in the strain vectors $\mathcal{L}_{eq}$ and $\mathcal{L}_{bc}$ (see Eqs. (6) and (7), respectively). Thus, elements along the rows of the stiffness matrices, where each row corresponds to a unique equilibrium equation at a discretisation grid point, can vary by orders of magnitude and lead to a large condition number. The use of the compliance matrix $\boldsymbol{s}$ is an inherent numerical drawback of the chosen theoretical framework in terms of solving the problem numerically using the DQM. This drawback can be partially remedied by

[1] Runge's phenomenon is a problem of oscillation between discretisation points which occurs when high-order interpolation polynomials are used in a grid of uniformly spaced points. Thus, increasing the interpolation order of the polynomial on a uniform grid spacing does not necessarily lead to better numerical solutions. The Chebychev-Gauss-Lobatto grid, on the other hand, guarantees that the maximum error reduces with increasing polynomial order.

[2] In linear algebra, the condition number of a matrix is a metric to gauge how sensitive the solution to a system of linear equations is to errors in the inputs. Thus, the condition number indicates the expected accuracy of matrix inversion and of the solution. In general, the condition number $\kappa$ of a matrix $\boldsymbol{A}$ is given by the product of two norms $\kappa(\boldsymbol{A}) = \|\boldsymbol{A}^{-1}\| \cdot \|\boldsymbol{A}\|$, such that by definition $\kappa(\boldsymbol{A}) \geq 1$ with values near unity indicating a well-conditioned matrix [45, p. 321].

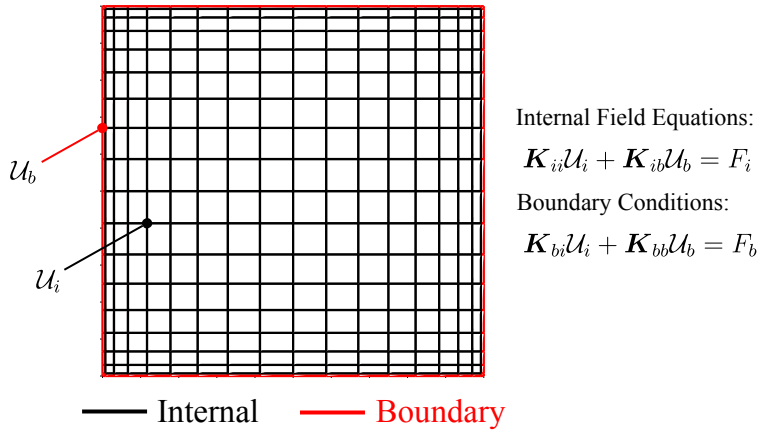


**Figure 16:** A non-uniform Chebychev-Gauss-Lobatto grid broken into a set of internal grid points and a grid of boundary points. The governing field equations are only applied at the internal points and the boundary conditions only at the boundary points. Thus, the problem is substructured into four unique matrices and solved for the field and boundary unknowns $\mathcal{U}_i$ and $\mathcal{U}_b$, respectively.

normalising each row $K_r$ of the stiffness matrix, i.e. each equilibrium equation, using the root-mean-square of the corresponding row,

$$K_r^n = \frac{K_r}{\sqrt{\sum_c K_{rc}^2}} \tag{22}$$

where $K_{rc}$ are the $c$ components of row $K_r$, and $K_r^n$ is a normalised row.

Finally, the stiffness matrices in Eq. (21) are generally non-symmetric and can have zeros on the leading diagonal. This occurs because the in-plane and bending equilibrium equations Eqs. (4a) and (4b), as well as the enhanced constitutive equations Eq. (4c), are discretised into the same matrix due to the mixed displacement- and stress-based nature of the HR model. To overcome the issue of zeros on the leading diagonal, the idea of damping, as proposed in the works of Levenberg [46] and Marquardt [47], is used, by replacing the zeros with small terms of magnitude $10^{-10}$. Even though this method considerably reduces the condition number of the stiffness matrix, the authors are aware that damping the diagonal in this manner perturbs the underlying numerical problem and more elegant solutions may be possible. Second, the matrix inversion is not computed using the backslash operator in MATLAB, but rather with the Moore-Penrose pseudoinverse as detailed in reference [48]. One possible solution is to discretise the plate into multiple DQM elements using the method proposed by Tornabene et al. [43]. Such an approach is equivalent to a strong-form FEM and considerably reduces the bandwidth of the matrices to improve the conditioning of the stiffness matrix.

As Pagano's 3D elasticity solution [35] is only valid for simply supported orthotropic plates, a 3D FEM model is used to benchmark the HR model results for anisotropic laminates. The plate is modelled in the commercial software package Abaqus using a 3D body that is 1 m long, 50 mm thick and 1 m wide. This plate, with characteristic length to thickness aspect ratio of $a/t = 20$, is meshed with 784,080 linear C3D8R reduced integration brick elements with enhanced hourglassing control, i.e. 80 elements through the thickness and 99 elements in both in-plane dimensions. This choice was based on initial convergence criteria and on the constraint of keeping the runtime at less than 12 hrs. In Section 2.2.2, laminates with up to eight unique layers are analysed such that each laminate features a minimum of ten elements per layer. A pressure loading of $\hat{P}_t = -100$ kPa and a shear traction of $\hat{T}_{tx} = -50$ kPa are applied on the top surface. Finally, all six degrees of freedom (three translations and three rotations) are constrained at the four clamped edges throughout the entire plate cross-section. With 810,000 nodes and six degrees of freedom per node (4.86 million variables) the run-time on the local desktop PC equipped with an Intel i7-2600S processor with 2.80 GHz and 8 GB of RAM is about 12 hrs, whereas the HR3 (15 variables) and HR3-RZT (19 variables) codes in MATLAB have run-times of around 120 sec and 180 sec, respectively, at the chosen mesh size of 361 grid points (5,415 and 6,859 variables, respectively). Thus, the HR model in MATLAB reduces the number of degrees of freedom by three orders of magnitude compared to the 3D FEM model in Abaqus. However, it must be noted that the runtime in Abaqus is highly dependent on the available RAM and not the CPU speed. Therefore, the Abaqus model can be sped-up considerably if the available RAM is increased.

### *2.2.2. Model validation*

To test the general applicability of the HR formulation a variety of different symmetric and non-symmetric composite laminates and sandwich plates are tested. The two materials used throughout the analysis are as defined in Table 1 of Section 2.1.2. The stacking sequences of differ-

**Table 7:** Analysed anisotropic stacking sequences. Subscripts indicate the repetition of a property over the corresponding number of layers. Layer thicknesses stated as ratios of total laminate thickness.

| Laminate | Thickness Ratio | Material | Stacking Sequence |
|---|---|---|---|
| E | $[0.25_4]$ | $[\mathrm{c}_4]$ | $[45/-45/0/90]$ |
| F | $[0.2_5]$ | $[\mathrm{c}_5]$ | $[60/30/75/30/60]$ |
| G | $[0.125_2/0.5/0.125_2]$ | $[\mathrm{c}_2/\mathrm{h}/\mathrm{c}_2]$ | $[45/-45/0/0/90]$ |
| H | $[(1/12)_3/0.5/(1/12)_3]$ | $[\mathrm{c}_3/\mathrm{h}/\mathrm{c}_3]$ | $[15/75/45/0/45/75/15]$ |

ent laminates including layer orientations, layer thickness and layer material codes are summarised in Table 7. All laminates have a total thickness of 50 mm, i.e. $a/t = 20$.

Laminates E and F are general composite laminates with orthotropic and off-axis plies with respect to the $(x, y)$ coordinate system. Laminate E is a balanced, non-symmetric laminate that exhibits in-plane/out-of-plane coupling and bend/twist coupling. Laminate F is an unbalanced, symmetric laminate which exhibits both extension/shear and bend/twist coupling. Laminates G and H extend the two coupling mechanisms mentioned above to a soft-core sandwich plate that accentuates the ZZ effect. Thus, these two latter test cases represent non-classical laminates with arbitrary fibre orientations and material heterogeneity, which intend to test the full capability of the different HR models.

Henceforth, all deflection and stress results are presented in normalised form. The same definitions of the normalised metrics as previously defined in Eq. (17) are used, but due to the change in load case the factor $p_0$ in the denominators of the metrics is replaced by the norm $\sqrt{p_0^2 + t_0^2}$. Furthermore, the transverse shear stresses $\sigma_{xz}$ and $\sigma_{yz}$ are no longer computed at the edges of the plate, as this represents a singularity in the 3D FEM model, but at the quarterspan. Hence, the new definition of the stress metrics is given by

$$
\begin{aligned}
\bar{w}_0 &= \frac{E_2^{(c)} t^2}{a^2 b^2 \sqrt{p_0^2 + t_0^2}} \int_{-\frac{t}{2}}^{\frac{t}{2}} u_z \left( \frac{a}{2}, \frac{b}{2}, z \right) \mathrm{d}z, \\
\bar{\sigma}_x(z) &= \frac{t^2}{a^2 \sqrt{p_0^2 + t_0^2}} \sigma_x \left( \frac{a}{2}, \frac{b}{2}, z \right), \\
\bar{\sigma}_y(z) &= \frac{t^2}{b^2 \sqrt{p_0^2 + t_0^2}} \sigma_y \left( \frac{a}{2}, \frac{b}{2}, z \right), \\
\bar{\sigma}_z(z) &= \frac{1}{\sqrt{p_0^2 + t_0^2}} \sigma_z \left( \frac{a}{2}, \frac{b}{2}, z \right), \\
\bar{\sigma}_{xy}(z) &= \frac{t^2}{ab \sqrt{p_0^2 + t_0^2}} \sigma_{xy} \left( \frac{a}{4}, \frac{b}{4}, z \right), \\
\bar{\sigma}_{xz}(z) &= \frac{1}{\sqrt{p_0^2 + t_0^2}} \sigma_{xz} \left( \frac{a}{4}, \frac{b}{2}, z \right), \\
\bar{\sigma}_{yz}(z) &= \frac{1}{\sqrt{p_0^2 + t_0^2}} \sigma_{yz} \left( \frac{a}{2}, \frac{b}{4}, z \right).
\end{aligned}
\tag{23}
$$

The normalised deflection $\bar{w}_0$ for the HR models is compared against the normalised average through-thickness deflection of the 3D model.

The accuracy of the different HR models in predicting the bending deflection of laminates E-H, with characteristic length to thickness ratio $a/t = 20$, under the load case defined in Figure 15 is presented in Table 8. The table summarises the percentage error in the maximum normalised bending deflection $|\bar{w}_0|$ to four significant figures with respect to the 3D FEM result. The results show that the models with and without ZZ functionality predict the bending deflection to within 1% of the 3D FEM solution, with the exception of a 2.59% error in the HR3-RZT model for laminate F.

There are two possible explanations for the larger discrepancy of the HR3-RZT result for laminate F. A possible first source of error is the numerical conditioning of the problem. However, as shown in Table 9, the condition number $\kappa$ of the DQM stiffness matrix $\boldsymbol{K}$ is of equal magnitude as $\kappa(\boldsymbol{K})$ of HR3-RZTmx, and in fact slightly less than the condition number for HR3. In all cases, the condition number is relatively high, and as discussed in Section 2.2.1, future work should focus on strategies to reduce $\kappa(\boldsymbol{K})$. One possible solution is to reduce the bandwidth of the matrices, either by using localised DQ methods or by implementing the strong-form DQ finite element method developed by Tornabene and co-workers [43]. An alternative would be to transform the governing differential equations Eqs. (4) into the weak form by using the generalised Galerkin method. One drawback of this latter approach is that derivatives used to compute the stresses are not calculated as accurately using $C^0$ continuous finite elements as they are with DQ weighting matrices in the strong-form FEM.

A second source of error in the HR3-RZT model is that it does not account for EWLs. As the error in the HR3 model for laminate F is small (0.23%) and the presence of EWLs only influences the definition of the ZZ function, which is not included in HR3, it is possible that failing to account for EWLs artificially alters the stiffness of the structure. This explanation is likely as the HR3-RZTmx model, which does account for EWLs, reduces the error by a factor of three. Furthermore, the through-thickness plots of the two transverse shear stress metrics $\bar{\sigma}_{xz}$ and $\bar{\sigma}_{yz}$ in Figure 22 show that the HR3-RZT solution does not exactly correlate with the 3D FEM solution, whereas the other three HR models are almost coincident with the

**Table 8:** Anisotropic laminates E-H with $a/t = 20$: Percentage error in normalised bending deflection $|\bar{w}_0|$ to four significant figures for different HR models with respect to a 3D FEM solution.

| | **Laminate E** | **Laminate F** | **Laminate G** | **Laminate H** |
|---|---|---|---|---|
| **3D FEM** | **0.002525** | **0.002613** | **0.004148** | **0.004282** |
| HR3 (%) | 0.18 | 0.23 | 0.04 | 0.20 |
| HR3-RZT (%) | 0.06 | 2.59 | -0.05 | -0.38 |
| HR3-RZTmx (%) | 0.19 | 0.80 | -0.09 | -0.21 |
| HR3-MZZF (%) | 0.13 | 0.06 | -0.08 | 0.15 |

**Table 9:** Laminate F: Condition number $\kappa$ of the DQM stiffness matrix $\boldsymbol{K}$ that is inverted to solved the structural problem.

| | HR3 | HR3-RZT | HR3-RZTmx | HR3-MZZF |
|---|---|---|---|---|
| $\kappa(\boldsymbol{K})$ | $1.929 \times 10^{16}$ | $1.367 \times 10^{16}$ | $1.326 \times 10^{16}$ | $1.391 \times 10^{16}$ |

benchmark. As the ZZ effect, and by extension the influence of EWLs, arises from differences in the transverse shear moduli, the results suggest that the discrepancy in the HR3-RZT model is due to a failure to account for EWLs. Thus, the modified RZT ZZ function implemented in HR3-RZTmx is recommended for most accurate results.

To compare the accuracy of the HR 3D stress fields, the through-thickness variations of all six stress metrics are plotted in Figures 17-28 for the characteristic length to thickness ratio $a/t = 20$. The in-plane $(x, y)$ locations of each $z$-wise plot are given in the stress metric definitions of Eq. (23) and are also indicated in the figure captions.

For all laminates investigated herein, the HR3, HR3-RZTmx and HR3-MZZF model results follow the 3D FEM solutions closely throughout the entire thickness. The HR3-RZT model also correlates well with the 3D FEM solution for most laminates with the exception of the transverse shear stresses for laminate F (Figure 22). As previously discussed, this inaccuracy arises because the HR3-RZT model does not account for EWLs in the definition of the RZT ZZ function, and is therefore less robust than the modified HR3-RZTmx model.

The through-thickness plots support the findings of Table 8 that both the HR3 model without ZZ functionality and the HR3 ZZ models accurately predict the structural behaviour of the anisotropic laminates. As shown in Figures 17-19 and Figures 20-22 the HR3 model remains accurate for the anisotropic composite laminates E and F. In general, most composite laminae have $G_{13} < G_{23}$ such that the maximum and minimum values of transverse shear stiffness occur for $0^\circ$ and $90^\circ$ plies, respectively. Thus, the HR3 model is expected to be more accurate for general anisotropic than for orthotropic $0/90$ laminates, as the layerwise differences in transverse shear moduli is reduced. However, for sandwich laminate H the HR3 model is less accurate than the HR3-RZTmx model, with the discrepancies especially pronounced for the in-plane shear stress plot in Figure 27b.

As for the orthotropic laminates investigated in Section 2.1.2, the HR3-RZTmx model most consistently correlates with the 3D benchmark solution for the full range of anisotropic laminates investigated. The only marked discrepancy between the 3D FEM solution and the HR3-RZTmx model, and in fact all other HR models, is the in-plane shear stress $\bar{\sigma}_{xy}$ for laminate F shown in Figure 21b. To ascertain which of these stress fields, the 3D FEM or the HR solutions, is the most accurate result, the residuals in Cauchy's $x$- and $y$-direction equilibrium equations are calculated. Only these two equilibrium equations explicitly contain the in-plane shear stress $\sigma_{xy}$. Furthermore, as the 3D FEM and HR solutions of the two in-plane stresses $\sigma_x$ and $\sigma_y$, and the two transverse shear stresses $\sigma_{xz}$ and $\sigma_{yz}$ are well correlated, the model that satisfies Cauchy's equilibrium equations with the least residual is deemed to be the most accurate. Hence, the two normalised residuals

$$\bar{R}_x\left(\frac{a}{4}, \frac{b}{4}, z\right) = \frac{1}{\sqrt{p_0^2 + t_0^2}} \left[\frac{\partial \sigma_x}{\partial x} + \frac{\partial \sigma_{xy}}{\partial y} + \frac{\partial \sigma_{xz}}{\partial z}\right]\Bigg|_{\substack{x=\frac{a}{4} \\ y=\frac{b}{4}}} \tag{24a}$$

$$\bar{R}_y\left(\frac{a}{4}, \frac{b}{4}, z\right) = \frac{1}{\sqrt{p_0^2 + t_0^2}} \left[\frac{\partial \sigma_{xy}}{\partial x} + \frac{\partial \sigma_y}{\partial y} + \frac{\partial \sigma_{yz}}{\partial z}\right]\Bigg|_{\substack{x=\frac{a}{4} \\ y=\frac{b}{4}}} \tag{24b}$$

are used to compare the accuracy of the in-plane shear stress field $\sigma_{xy}$ of laminate F at $\left(\frac{a}{4}, \frac{b}{4}, z\right)$. The 3D FEM stress results are extracted from Abaqus using a Python script and then post-processed in MATLAB using the internal `gradient` function to calculate the derivatives in Eq. (24).

Figure 29 compares the normalised residuals $\bar{R}_x$ and $\bar{R}_y$ of 3D FEM and the HR3 model through the thickness of laminate F at $\left(\frac{a}{4}, \frac{b}{4}, z\right)$. The plots show that for all cases considered here, the residuals for the HR3 model are less than the residual for the 3D FEM model. Figure 30 shows that the residuals $\bar{R}_x$ and $\bar{R}_y$ for all four HR models

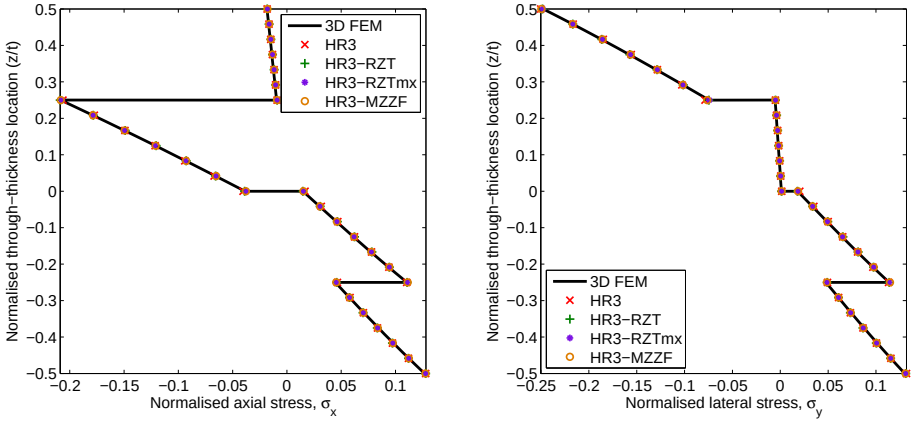


**(a)** Normalised axial stress, $\bar{\sigma}_x$ **(b)** Normalised lateral stress, $\bar{\sigma}_y$

**Figure 17:** Laminate E: Through-thickness distributions of the normalised axial ($\bar{\sigma}_x$) and lateral ($\bar{\sigma}_y$) stresses at $(a/2, b/2, z)$ for $a/t = 20$.

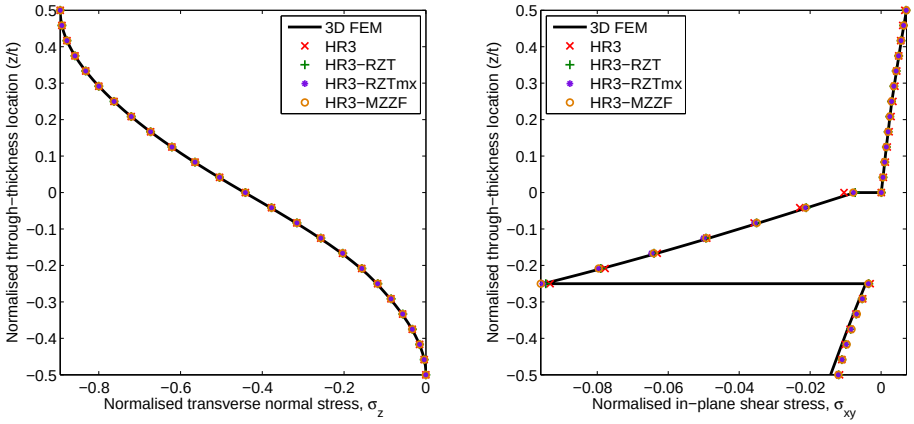


**(a)** Normalised transverse normal stress, $\bar{\sigma}_z$ **(b)** Normalised in-plane shear stress, $\bar{\sigma}_{xy}$

**Figure 18:** Laminate E: Through-thickness distributions of the normalised transverse normal ($\bar{\sigma}_z$) and in-plane shear ($\bar{\sigma}_{xy}$) stresses at $(a/2, b/2, z)$ and $(a/4, b/4, z)$, respectively for $a/t = 20$.

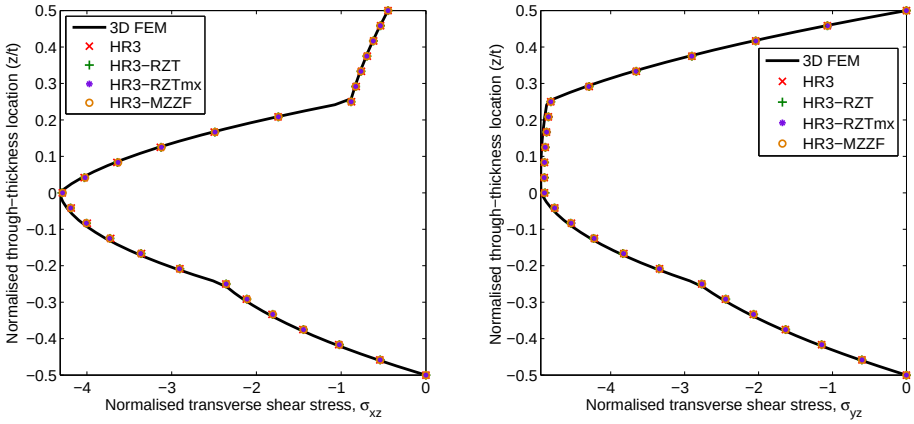


**(a)** Normalised transverse shear stress, $\bar{\sigma}_{xz}$ **(b)** Normalised transverse shear stress, $\bar{\sigma}_{yz}$

**Figure 19:** Laminate E: Through-thickness distributions of the normalised transverse shear stresses ($\bar{\sigma}_{xz}$ and $\bar{\sigma}_{yz}$) at $(a/4, b/2, z)$ and $(a/2, b/4, z)$, respectively for $a/t = 20$.

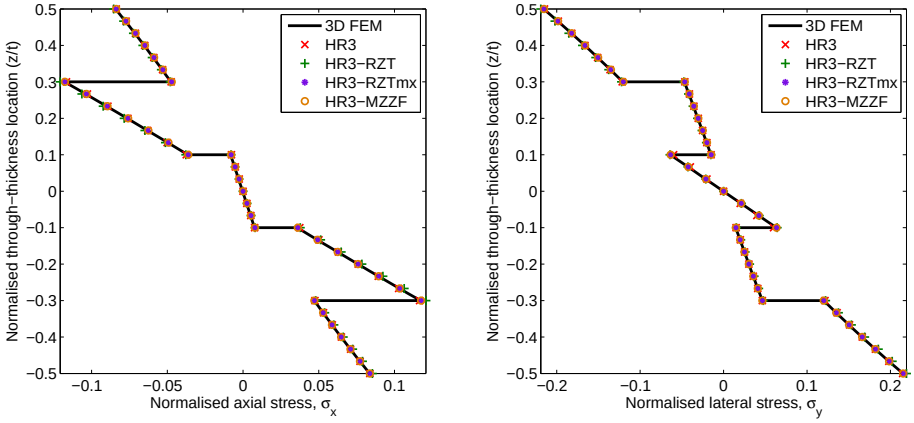


**(a)** Normalised axial stress, $\bar{\sigma}_x$ **(b)** Normalised lateral stress, $\bar{\sigma}_y$

**Figure 20:** Laminate F: Through-thickness distributions of the normalised axial ($\bar{\sigma}_x$) and lateral ($\bar{\sigma}_y$) stresses at $(a/2, b/2, z)$ for $a/t = 20$.

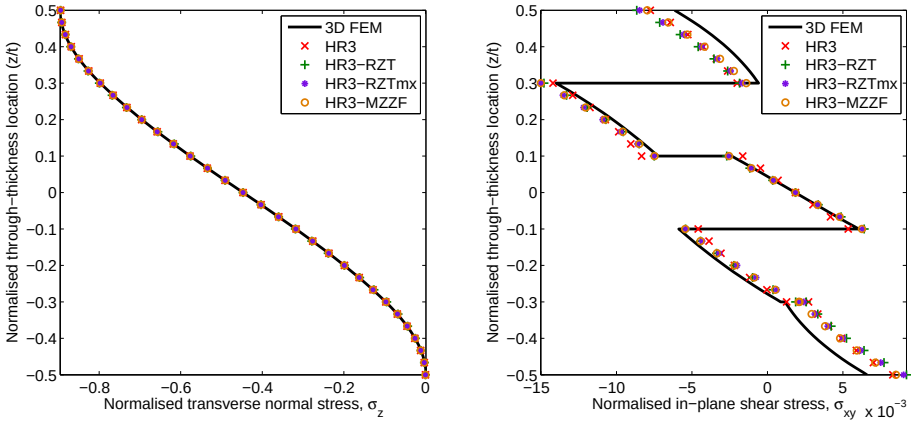


**(a)** Normalised transverse normal stress, $\bar{\sigma}_z$ **(b)** Normalised in-plane shear stress, $\bar{\sigma}_{xy}$

**Figure 21:** Laminate F: Through-thickness distributions of the normalised transverse normal ($\bar{\sigma}_z$) and in-plane shear ($\bar{\sigma}_{xy}$) stresses at $(a/2, b/2, z)$ and $(a/4, b/4, z)$, respectively for $a/t = 20$.

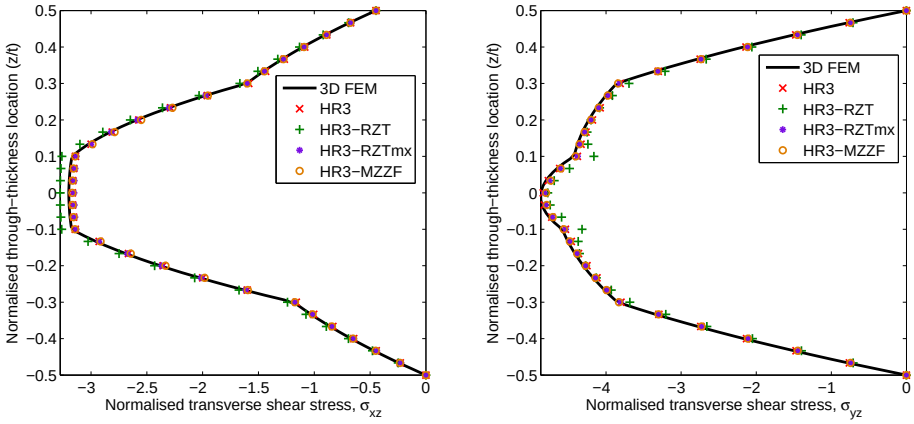


**(a)** Normalised transverse shear stress, $\bar{\sigma}_{xz}$ **(b)** Normalised transverse shear stress, $\bar{\sigma}_{yz}$

**Figure 22:** Laminate F: Through-thickness distributions of the normalised transverse shear stresses ($\bar{\sigma}_{xz}$ and $\bar{\sigma}_{yz}$) at $(a/4, b/2, z)$ and $(a/2, b/4, z)$, respectively for $a/t = 20$.

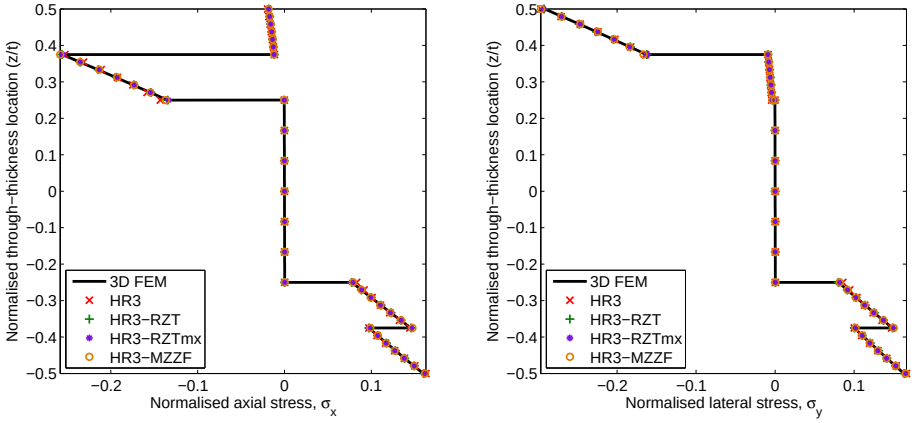


**(a)** Normalised axial stress, $\bar{\sigma}_x$ **(b)** Normalised lateral stress, $\bar{\sigma}_y$

**Figure 23:** Laminate G: Through-thickness distributions of the normalised axial ($\bar{\sigma}_x$) and lateral ($\bar{\sigma}_y$) stresses at $(a/2, b/2, z)$ for $a/t = 20$.

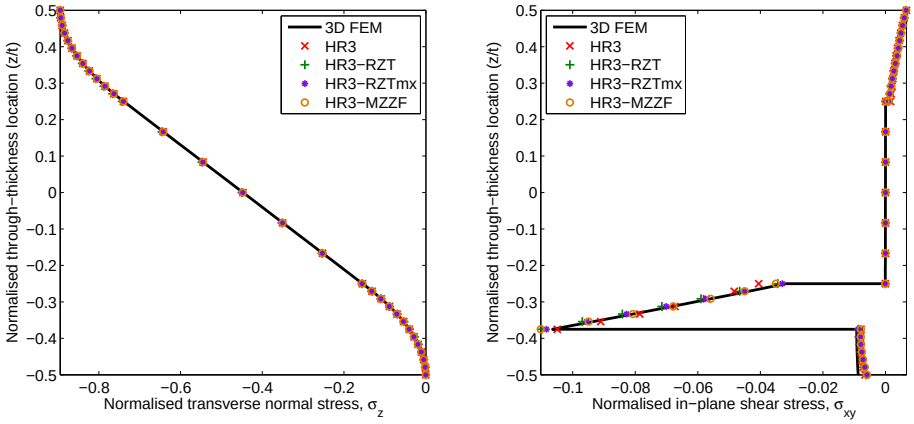


**(a)** Normalised transverse normal stress, $\bar{\sigma}_z$ **(b)** Normalised in-plane shear stress, $\bar{\sigma}_{xy}$

**Figure 24:** Laminate G: Through-thickness distributions of the normalised transverse normal ($\bar{\sigma}_z$) and in-plane shear ($\bar{\sigma}_{xy}$) stresses at $(a/2, b/2, z)$ and $(a/4, b/4, z)$, respectively for $a/t = 20$.

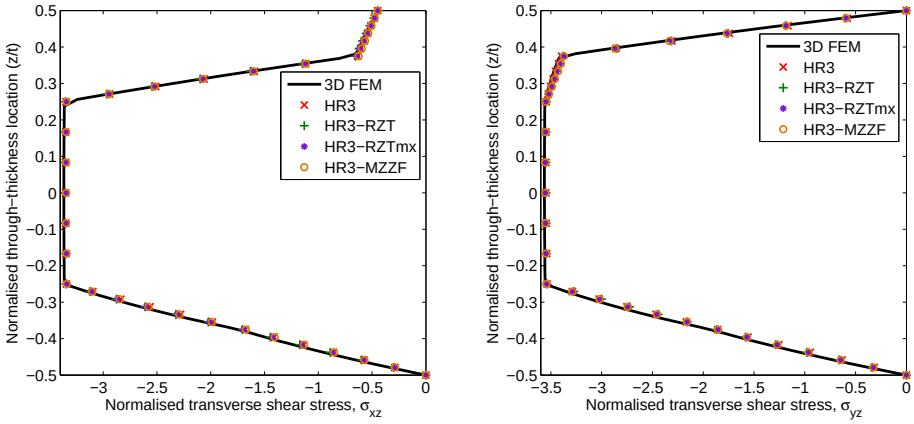


**(a)** Normalised transverse shear stress, $\bar{\sigma}_{xz}$ **(b)** Normalised transverse shear stress, $\bar{\sigma}_{yz}$

**Figure 25:** Laminate G: Through-thickness distributions of the normalised transverse shear stresses ($\bar{\sigma}_{xz}$ and $\bar{\sigma}_{yz}$) at $(a/4, b/2, z)$ and $(a/2, b/4, z)$, respectively for $a/t = 20$.

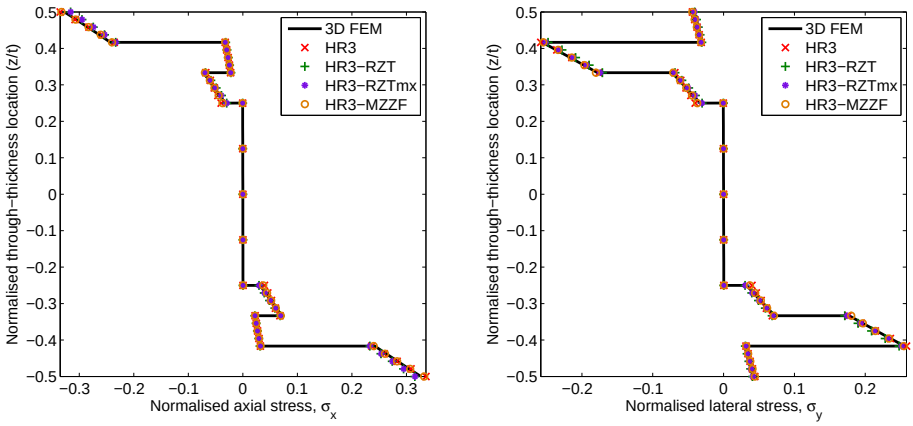


**(a)** Normalised axial stress, $\bar{\sigma}_x$ **(b)** Normalised lateral stress, $\bar{\sigma}_y$

**Figure 26:** Laminate H: Through-thickness distributions of the normalised axial ($\bar{\sigma}_x$) and lateral ($\bar{\sigma}_y$) stresses at $(a/2, b/2, z)$ for $a/t = 20$.

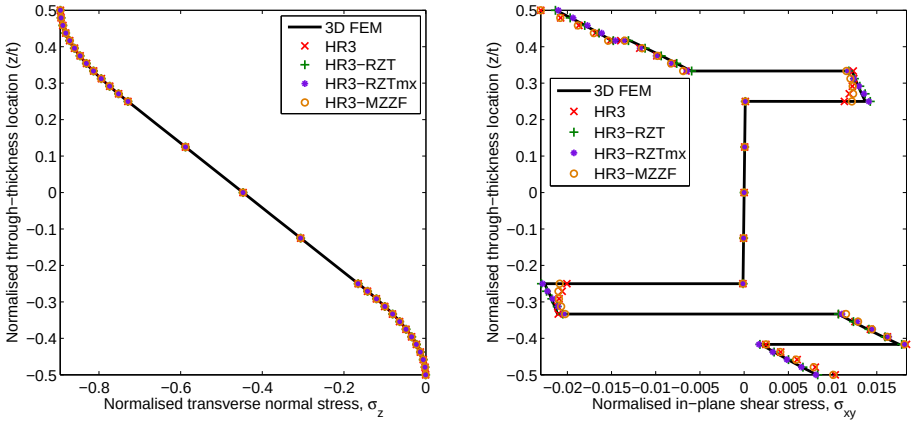


**(a)** Normalised transverse normal stress, $\bar{\sigma}_z$ **(b)** Normalised in-plane shear stress, $\bar{\sigma}_{xy}$

**Figure 27:** Laminate H: Through-thickness distributions of the normalised transverse normal ($\bar{\sigma}_z$) and in-plane shear ($\bar{\sigma}_{xy}$) stresses at $(a/2, b/2, z)$ and $(a/4, b/4, z)$, respectively for $a/t = 20$.

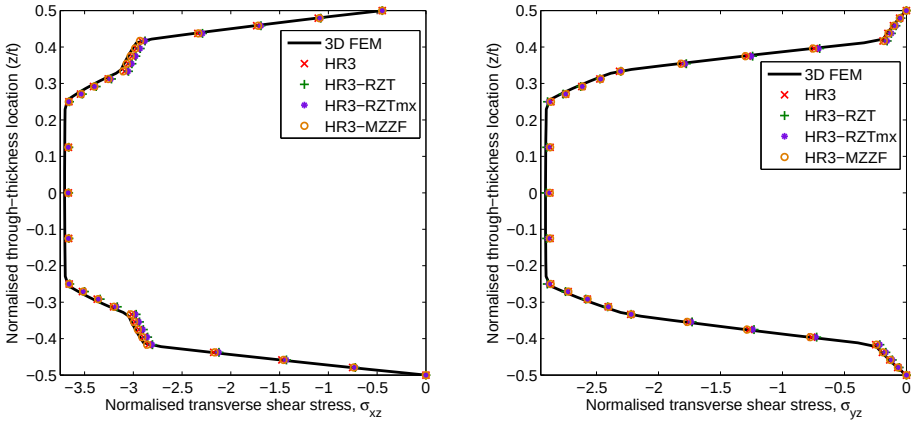


**(a)** Normalised transverse shear stress, $\bar{\sigma}_{xz}$ **(b)** Normalised transverse shear stress, $\bar{\sigma}_{yz}$

**Figure 28:** Laminate H: Through-thickness distributions of the normalised transverse shear stresses ($\bar{\sigma}_{xz}$ and $\bar{\sigma}_{yz}$) at $(a/4, b/2, z)$ and $(a/2, b/4, z)$, respectively for $a/t = 20$.

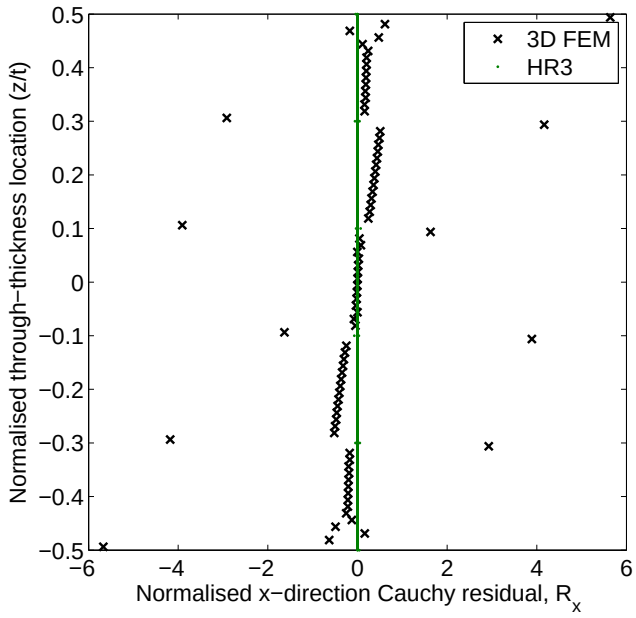


**(a)** Normalised $x$-direction Cauchy residual, $\bar{R}_x$

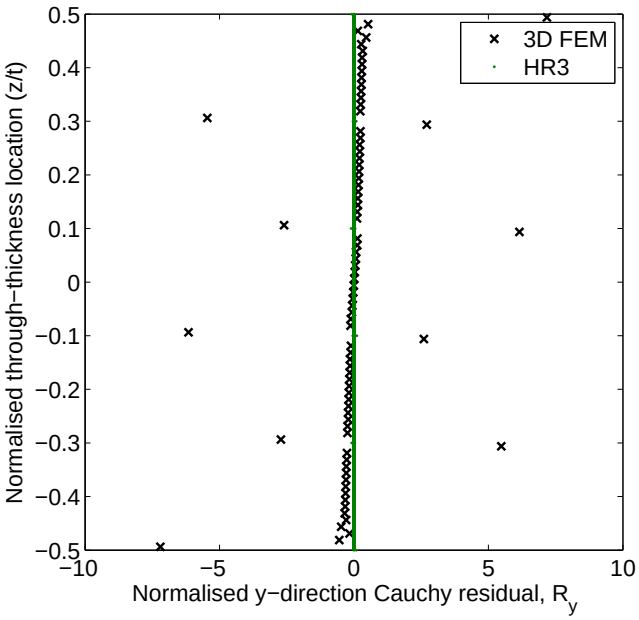


**(b)** Normalised $y$-direction Cauchy residual, $\bar{R}_y$

**Figure 29:** Laminate F: Normalised $x$-direction and $y$-direction Cauchy residuals $\bar{R}_x$ and $\bar{R}_y$, respectively, for 3D FEM and HR models at $(a/4, b/4, z)$ with $a/t = 20$.

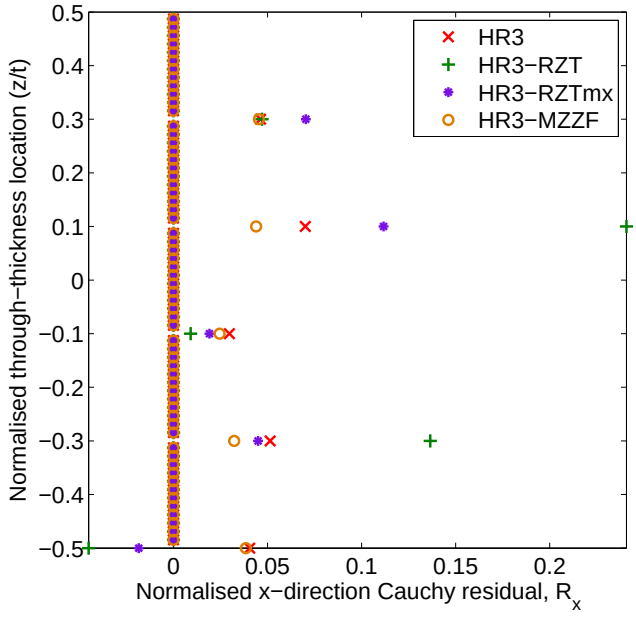


**(a)** Normalised $x$-direction Cauchy residual, $\bar{R}_x$

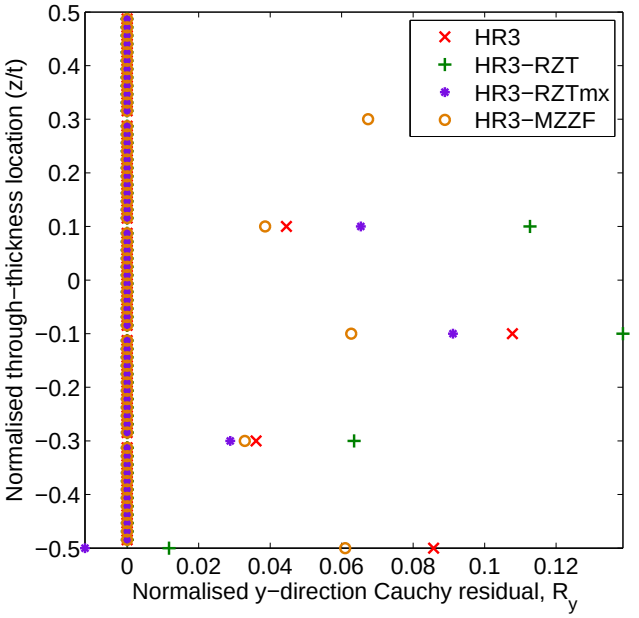


**(b)** Normalised $y$-direction Cauchy residual, $\bar{R}_y$

**Figure 30:** Laminate F: Normalised $x$-direction and $y$-direction Cauchy residuals $\bar{R}_x$ and $\bar{R}_y$, respectively, for all HR models at $(a/4, b/4, z)$ with $a/t = 20$.

are close to zero throughout the whole laminate thickness. For the 3D FEM and HR models, the maximum residuals occur at the ply interfaces due to the relatively higher numerical error associated with calculating derivatives at interval ends. The maximum error in the HR models at the ply interfaces is of order $10^{-1}$, whereas the maximum 3D FEM residual is almost two orders of magnitude greater, i.e. of the order of the applied loading norm $\sqrt{p_0^2 + t_0^2}$. In fact, remote from the layer interfaces the HR model residuals are of order $10^{-6}$ and therefore negligibly small compared to the loading norm.

Thus, even the detailed 3D FEM meshes considered here, with more than ten elements per layer and multiple hours of runtime on a high-performance computer, do not guarantee that Cauchy's equilibrium equations are satisfied with negligible error. The results in Figure 30 suggest that the HR formulation 3D stress fields equilibrate more accurately in Cauchy's equations than the 3D FEM stresses. At the same time the HR models reduce the number of variables by three orders of magnitude, thereby cutting the computational runtime from multiple hours to 1-2 minutes.

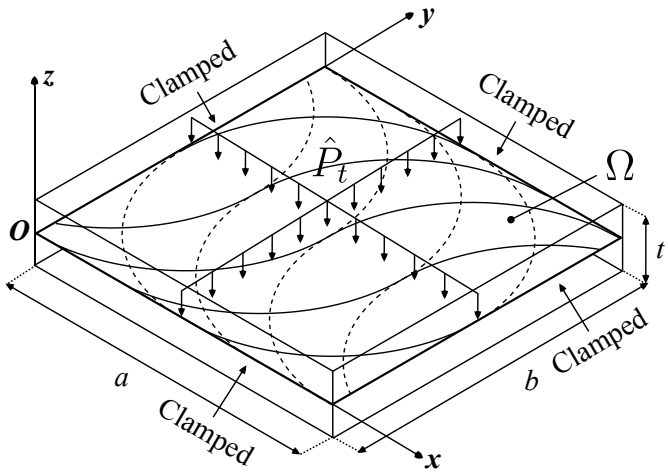


**Figure 31:** A composite plate with tow-steered fibre paths, loaded on the top surface by a uniformly distributed pressure load. All four edges are clamped. In the HR model, the 3D continuum is compressed onto an equivalent single layer Ω coincident with the midplane of the plate. For reference, the curvilinear fibre paths have been superimposed onto this equivalent single layer.

## 3. 3D stress fields in tow-steered laminates

In this section, the laminates considered are generalised further by allowing the fibre paths to vary continuously across the planform of the plate, i.e. with $(x, y)$ location. Thus, these laminates exhibit what is henceforth called *full 3D heterogeneity*, as the material properties can vary in both planar dimensions and through the thickness of the plate. The aim of this section is to benchmark the 3D stress fields in these tow-steered plates using the HR formulation and 3D FEM solutions.

### *3.1. Benchmarking of 3D stresses in tow-steered laminates*

Consider a square plate of unit in-plane dimensions $a = b = 1$ m and $t = 0.1$ m thickness $(a/t = 10)$ as depicted graphically in Figure 31. The plate comprises $N_l$ orthotropic, tow-steered laminae of arbitrary thickness $t^{(k)}$ with the fibre orientation $\alpha^{(k)}(x, y)$ varying smoothly over the planform of the plate. Due to the variable-stiffness design of the curvilinear tow paths, the reduced material stiffness matrix $\bar{\boldsymbol{Q}}^{(k)}(x, y)$ is a function of the in-plane location. As a result, the complete laminated plate has varying stiffness properties in all three Cartesian coordinates.

The individual tow-steered layers can be arranged in any general fashion but are assumed to be perfectly bonded, such that displacement and traction continuity at the interfaces is guaranteed. The plate is rigidly built-in along all four edges and is loaded via a uniformly distributed pressure $\hat{P}_t = p_0$ on the top surface. In reaction to the applied loading and constraining boundary conditions, the plate is assumed to deform isothermally into a new static equilibrium state.

In this work only linear fibre variations in one direction, i.e. prismatic variations, are considered. Such tow-steered fibre paths are conveniently defined using the notation of Gürdal and Olmedo [5],

$$\alpha(x, y) = \Phi\langle T_0 | T_1 \rangle \tag{25}$$

where $\Phi$ denotes the rotation of the fibre path with respect to the global $x$-axis, and angles $T_0$ and $T_1$ are the fibre directions at the ply centre and at a characteristic length $d$ from the centre, respectively, with respect to the global rotation $\Phi$. Thus, angle $\Phi$ also represents the direction of fibre variation. To cover the whole planform of the plate the fibre trajectories are shifted perpendicular to $\Phi$.

Manufacturing techniques that steer fibres by in-plane bending, such as AFP, inevitably cause gaps and overlaps when the reference path is shifted perpendicular to $\Phi$. The CTS technique, which steers fibre tows by in-plane shearing, allows the fibres to be tessellated without any gaps or overlaps, but induces an asymmetric variable thickness profile. Throughout this analysis the presence of tow gaps, tow overlaps and thickness variations is neglected as the main aim of the current work is to demonstrate the capability of modelling accurate 3D stresses for an idealised flat plate with variable stiffness. However, the HR models are readily extended to account for discrete or continuous thickness variations by locally changing the limits of through-thickness integration and by taking account of the ensuing curvature of the neutral axis [49].

The third-order model HR3 and third-order ZZ model HR3-MZZF are used to model the tow-steered plates. The

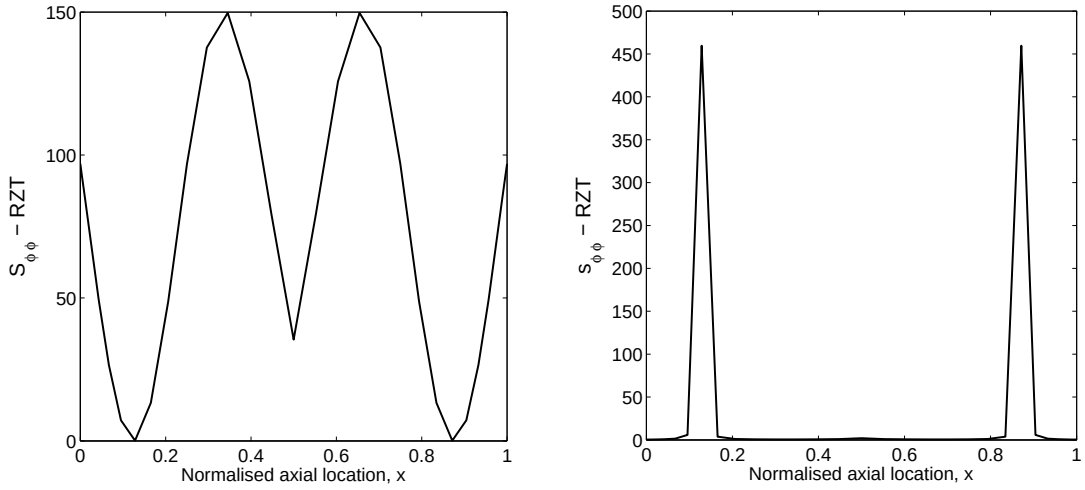


**(a)** $S_{\phi\phi}$ - RZT **(b)** $s_{\phi\phi}$ - RZT

**Figure 32:** Variation of ZZ stiffness term $S_{\phi\phi}$ and ZZ compliance term $s_{\phi\phi}$ of the HR3-RZT model along the length of a 1D beam with layup $[0 \pm \langle 90|0\rangle/0 \pm \langle 45|-45\rangle]_s$.

governing differential field equations (4) and boundary conditions (5) are converted into algebraic equations using the DQM approach outlined in Section 2.2.1. Thus, a system of algebraic equations in the form of Eqs. (21) is derived that is solved via standard matrix inversion, taking into account the normalisation of the equilibrium equations via Eq. (22).

In the present formulation, the RZT ZZ function can lead to certain numerical conditioning problems for variable-stiffness laminates when the governing equations are solved using the DQM. The RZT ZZ function varies over the planform of a variable-stiffness plate as it is based on actual transverse shear material properties. For a general fibre variation, the orthotropy in transverse shear moduli that drives the ZZ effect can be finite in some areas of the plate, but vanish locally if the layup is unidirectional or close to unidirectional at a specific point. Under these circumstances the RZT ZZ function vanishes and leads to numerical ill-conditioning in the matrix inversion $\boldsymbol{s} = \boldsymbol{S}^{-1}$ (See Figure 32).

Furthermore, it was found here that for variable-stiffness plates, the in-plane derivatives of the RZT ZZ function can vary significantly over the planform and thus lead to local singularities that ill-condition the DQ stiffness matrix. When using MZZF this is not an issue as this ZZ function is invariant with location $(x, y)$. Hence, due to the numerical ill-conditioning issues faced with the RZT ZZ function, the HR3-RZT and HR3-RZTmx models were not used for the variable-stiffness panels analysed in this section.

The ill-conditioning problem due to the in-plane derivatives of the RZT ZZ function may partially be remedied by using a local DQM approach, where only small number of grid points rather than the full domain is used to compute derivatives. Alternatively, the strong-form FEM by Tornabene et al. [43] may provide a similar solutions. Further investigating the numerical stability of the HR3-RZT model within a DQM framework should be the focus of future work.

Similar to Section 2.2.1, a 3D FEM model is used to benchmark the HR model results for the tow-steered laminates. After the plate geometry is meshed, a Python script is used to assign the pertinent material orientations to the elements depending on the exact location of the element centroid in 3D Cartesian space. To achieve converged results, the in-plane mesh density has to be increased to 149 elements in both in-plane directions to guarantee sufficiently smooth fibre variations from the discrete element angles in the $x$- and $y$-directions. Combined with 80 elements through the thickness, the 3D body is thus meshed with 1,776,080 linear C3D8R reduced integration brick elements with enhanced hourglassing control. Due to the high computational effort required, the Abaqus model was run on a high-performance computer with 128 GB of RAM. A pressure loading of $\hat{P}_t = -100$ kPa is applied on the top surface and all six degrees of freedom (three translations and three rotations) are constrained at the four clamped edges for all nodes throughout the entire plate cross-section.

The laminates investigated here are restricted to symmetrically laminated variable-stiffness composites and sandwich plates and are tabulated in Table 10. These laminates comprise the commonly used industrial material system IM7 8552 with $E_1 = 163$ GPa, $E_2 = E_3 = 12$ GPa, $G_{12} = 5$ GPa, $G_{13} = 4$ GPa, $G_{23} = 3.2$ GPa, $\upsilon_{12} = \upsilon_{13} = \upsilon_{23} = 0.3$, and the sandwich core h previously defined in Table 1. Laminates VAT A-C are tow-steered composite laminates, whereas laminate VAT D is a sandwich plate with tow-steered face sheets. The laminates have layers

**Table 10:** Analysed tow-steered stacking sequences. Subscripts indicate the repetition of a property over the corresponding number of layers. Layer thicknesses stated as ratios of total laminate thickness.

| Laminate | Thickness Ratio | Material | Stacking Sequence |
|---|---|---|---|
| VAT A | $[0.125_8]$ | $[\text{IM7}_8]$ | $[0 \pm \langle 0\|45\rangle/0 \pm \langle 90\|45\rangle]_s$ |
| VAT B | $[0.125_8]$ | $[\text{IM7}_8]$ | $[90 \pm \langle 0\|70\rangle/90 \pm \langle 90\|20\rangle]_s$ |
| VAT C | $[0.125_8]$ | $[\text{IM7}_8]$ | $[90 \pm \langle 0\|45\rangle/0 \pm \langle 45\|0\rangle]_s$ |
| VAT D | $[0.125_2/0.5/0.125_2]$ | $[\text{IM7}_2/\text{h}/\text{IM7}_2]$ | $[0 \pm \langle 90\|0\rangle/0/0 \mp \langle 90\|0\rangle]$ |

**Table 11:** Tow-steered laminates VAT A-D with $a/t = 10$: Percentage error in normalised bending deflection $|\bar{w}_0|$ to four significant figures for different HR models with respect to a 3D FEM solution.

| | VAT A | VAT B | VAT C | VAT D |
|---|---|---|---|---|
| **3D FEM** | **.003857** | **.003265** | **.003427** | **.01039** |
| HR3 (%) | 0.15 | 0.22 | 0.18 | 3.72 |
| HR3-MZZF (%) | 0.15 | 0.22 | 0.18 | -0.25 |

with fibre variations that vary explicitly in the $x$-direction (laminates VAT A and VAT D), $y$-direction (laminate VAT B) or both directions (laminate VAT C).

All deflection and stress results are presented as normalised metrics. The same definitions and spatial locations of the normalised metrics as previously defined in Eq. (23) is used. Due to the change in load case the factor $t_0 = 0$ in the denominators of the metrics. The accuracy of the different HR models in predicting the bending deflection of laminates VAT A-VAT D, with characteristic length to thickness ratio $a/t = 10$ under the load case defined in Figure 31, is presented in Table 11. The table summarises the percentage error in the maximum normalised bending deflection $|\bar{w}_0|$ to four significant figures with respect to the 3D FEM result. The results show that the models with and without ZZ functionality predict the bending deflection to within 1% of the 3D FEM solution for the variable-stiffness composites laminates VAT A-VAT C. For the variable-stiffness sandwich plate VAT D the maximum error in the HR3 model (3.72%) is greater than for the HR3-MZZF model. As was previously shown for orthotropic and anisotropic straight-fibre laminates in Sections 2.1.2 and 2.2.2, the inclusion of ZZ functionality is important for accurate modelling of sandwich panels.

Next, consider the through-thickness variations of all six stress metrics for laminates VAT A-VAT D as plotted in Figures 33-44 for the characteristic length to thickness ratio $a/t = 10$. The in-plane $(x, y)$ locations of each $z$-wise plot are given in the stress metric definitions of Eq. (23) and are also indicated in the figure captions. For the variable-stiffness composite laminates VAT A-VAT C both the HR3 and HR3-MZZF model results closely correlate the 3D FEM solutions throughout the entire thickness.

The plots for laminate VAT D in Figures 42-44 confirm the inferior accuracy of the HR3 model in modelling sandwich panels previously observed for the deflection results in Table 11. For laminate VAT D, both the in-plane stress plots for $\bar{\sigma}_x$ (Figure 42a), $\bar{\sigma}_y$ (Figure 42b) and $\bar{\sigma}_{xy}$ (Figure 43b), as well as the transverse shear plots for $\bar{\sigma}_{xz}$ (Figure 44a) and $\bar{\sigma}_{yz}$ (Figure 44b) show inaccuracies of 5-16% in the HR3 results compared to 3D FEM. The HR3-MZZF model follows the 3D FEM results more closely, with a maximum through-thickness error ranging from 1.5% for $\sigma_{xz}$ to 8% for $\sigma_{xy}$.

As previously observed in Section 2.2.2, the in-plane shear stresses $\bar{\sigma}_{xy}$ are generally the worst-matching plots for the laminates investigated. For example, consider the in-plane shear stress distribution for VAT B in Figure 37b. For four plies, the HR and 3D FEM results closely match, but show some differences for the central two layers and the two surface layers. The other stress fields that equilibrate the in-plane shear stress in Cauchy's $x$-direction equilibrium equations, $\sigma_x$ and $\sigma_{xz}$, and Cauchy's $y$-direction equilibrium equations, $\sigma_y$ and $\sigma_{yz}$, are closely correlated. Thus, as introduced in Section 2.2.2, the extent to which the 3D FEM and HR stress fields satisfy Cauchy's $x$- and $y$-direction equilibrium equations is ascertained using a metric capturing the general accuracy of the stress fields. Hence, the two normalised residuals in Eq. (24) are used to compare the accuracy of the in-plane shear stress field $\sigma_{xy}$ of laminate VAT B at $\left(\frac{a}{4}, \frac{b}{4}, z\right)$.

Figure 45 compares the normalised residuals $\bar{R}_x$ and $\bar{R}_y$ of 3D FEM and the HR3 model through the thickness of laminate VAT B at $\left(\frac{a}{4}, \frac{b}{4}, z\right)$. For all cases considered here, the residuals for the HR3 model are less than the residuals in the 3D FEM model. Furthermore, Figure 46 shows that the residuals $\bar{R}_x$ and $\bar{R}_y$ for both HR models are close to zero throughout the entire laminate thickness. The maximum residual in the HR models at the ply interfaces is of order $10^{-2}$ and reduces to $10^{-6}$ away from the interfaces. The maximum 3D FEM residual at the ply interfaces is of the order of the applied loading norm $p_0$, which is four orders of magnitude greater than the HR models, and even at layer midplane level the residual can be of order $10^{-2}$.

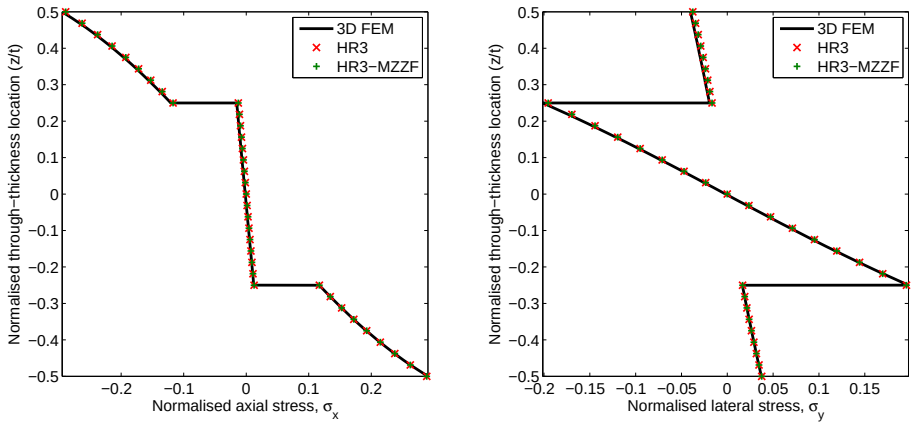


**(a)** Normalised axial stress, $\bar{\sigma}_x$ **(b)** Normalised lateral stress, $\bar{\sigma}_y$

**Figure 33:** Laminate VAT A: Through-thickness distributions of the normalised axial ($\bar{\sigma}_x$) and lateral ($\bar{\sigma}_y$) stresses at $(a/2, b/2, z)$ for $a/t = 10$.

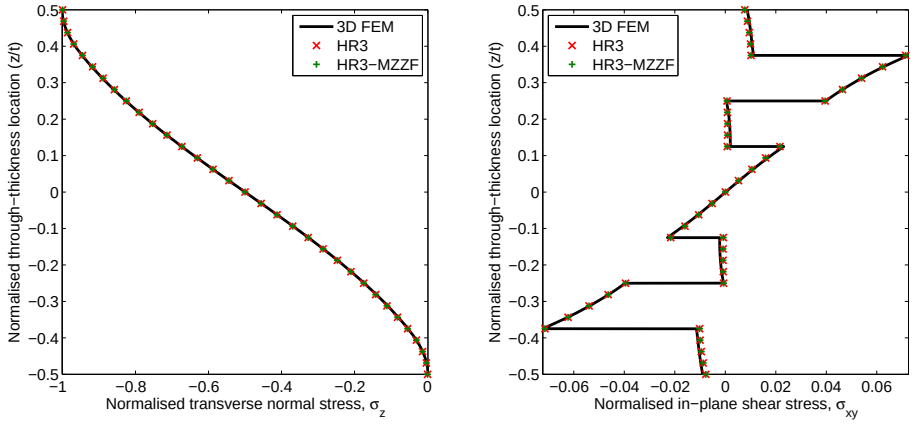


**(a)** Normalised transverse normal stress, $\bar{\sigma}_z$ **(b)** Normalised in-plane shear stress, $\bar{\sigma}_{xy}$

**Figure 34:** Laminate VAT A: Through-thickness distributions of the normalised transverse normal ($\bar{\sigma}_z$) and in-plane shear ($\bar{\sigma}_{xy}$) stresses at $(a/2, b/2, z)$ and $(a/4, b/4, z)$, respectively for $a/t = 10$.

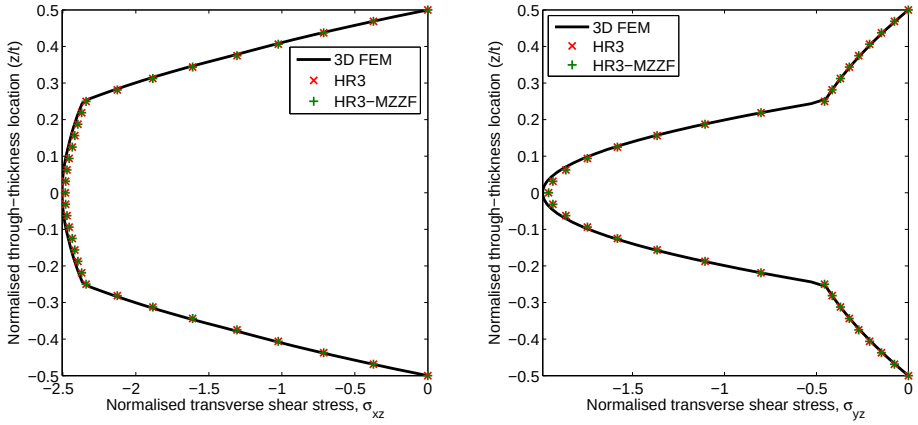


**(a)** Normalised transverse shear stress, $\bar{\sigma}_{xz}$ **(b)** Normalised transverse shear stress, $\bar{\sigma}_{yz}$

**Figure 35:** Laminate VAT A: Through-thickness distributions of the normalised transverse shear stresses ($\bar{\sigma}_{xz}$ and $\bar{\sigma}_{yz}$) at $(a/4, b/2, z)$ and $(a/2, b/4, z)$, respectively for $a/t = 10$.

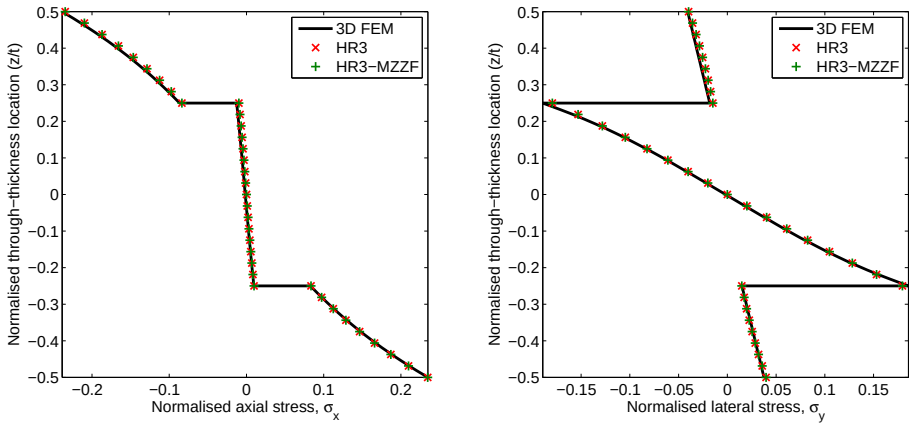


**(a)** Normalised axial stress, $\bar{\sigma}_x$ **(b)** Normalised lateral stress, $\bar{\sigma}_y$

**Figure 36:** Laminate VAT B: Through-thickness distributions of the normalised axial ($\bar{\sigma}_x$) and lateral ($\bar{\sigma}_y$) stresses at $(a/2, b/2, z)$ for $a/t = 10$.

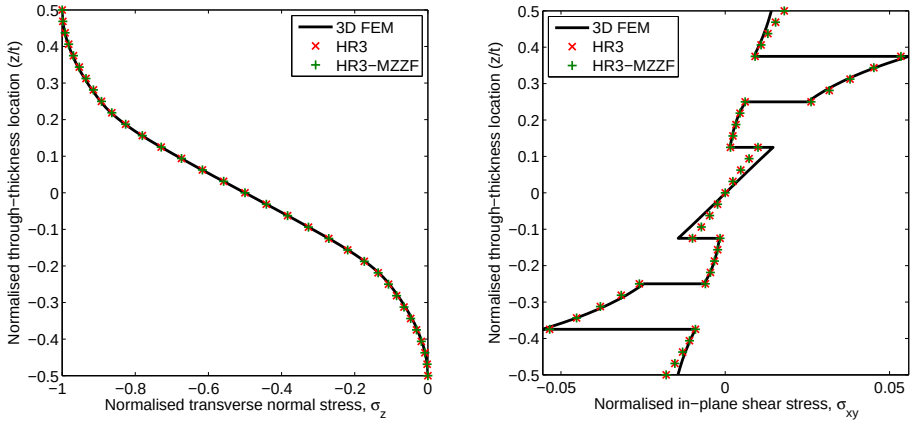


**(a)** Normalised transverse normal stress, $\bar{\sigma}_z$ **(b)** Normalised in-plane shear stress, $\bar{\sigma}_{xy}$

**Figure 37:** Laminate VAT B: Through-thickness distributions of the normalised transverse normal ($\bar{\sigma}_z$) and in-plane shear ($\bar{\sigma}_{xy}$) stresses at $(a/2, b/2, z)$ and $(a/4, b/4, z)$, respectively for $a/t = 10$.

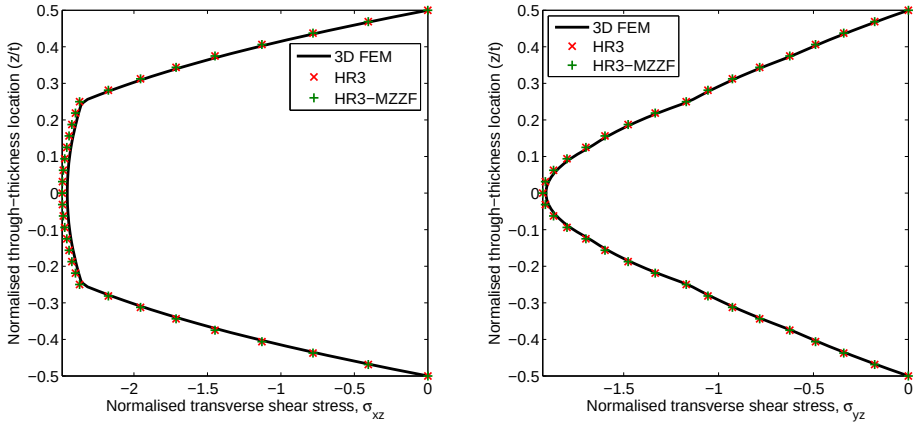


**(a)** Normalised transverse shear stress, $\bar{\sigma}_{xz}$ **(b)** Normalised transverse shear stress, $\bar{\sigma}_{yz}$

**Figure 38:** Laminate VAT B: Through-thickness distributions of the normalised transverse shear stresses ($\bar{\sigma}_{xz}$ and $\bar{\sigma}_{yz}$) at $(a/4, b/2, z)$ and $(a/2, b/4, z)$, respectively for $a/t = 10$.

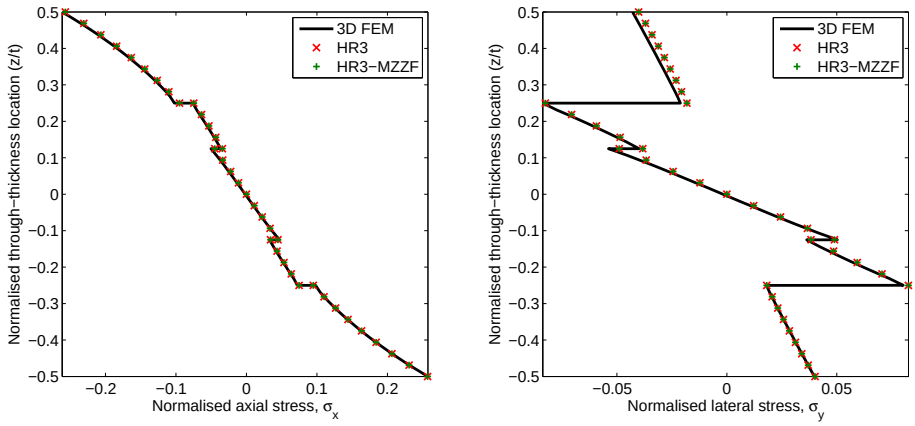


**(a)** Normalised axial stress, $\bar{\sigma}_x$ **(b)** Normalised lateral stress, $\bar{\sigma}_y$

**Figure 39:** Laminate VAT C: Through-thickness distributions of the normalised axial ($\bar{\sigma}_x$) and lateral ($\bar{\sigma}_y$) stresses at $(a/2, b/2, z)$ for $a/t = 10$.

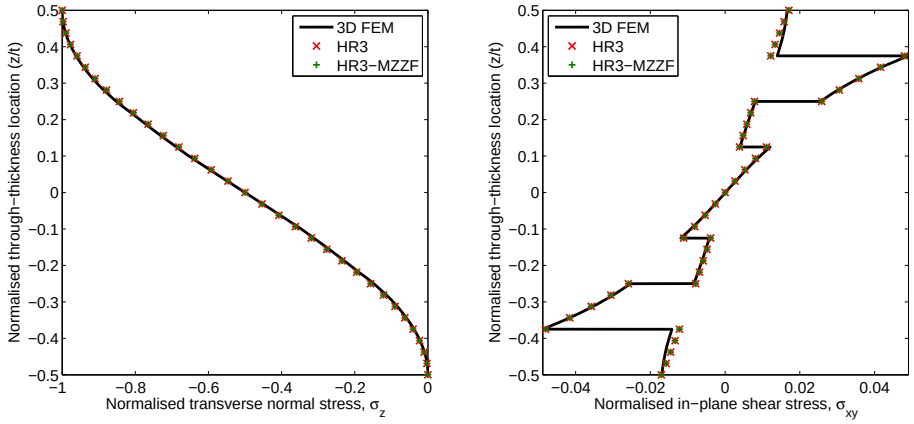


**(a)** Normalised transverse normal stress, $\bar{\sigma}_z$ **(b)** Normalised in-plane shear stress, $\bar{\sigma}_{xy}$

**Figure 40:** Laminate VAT C: Through-thickness distributions of the normalised transverse normal ($\bar{\sigma}_z$) and in-plane shear ($\bar{\sigma}_{xy}$) stresses at $(a/2, b/2, z)$ and $(a/4, b/4, z)$, respectively for $a/t = 10$.

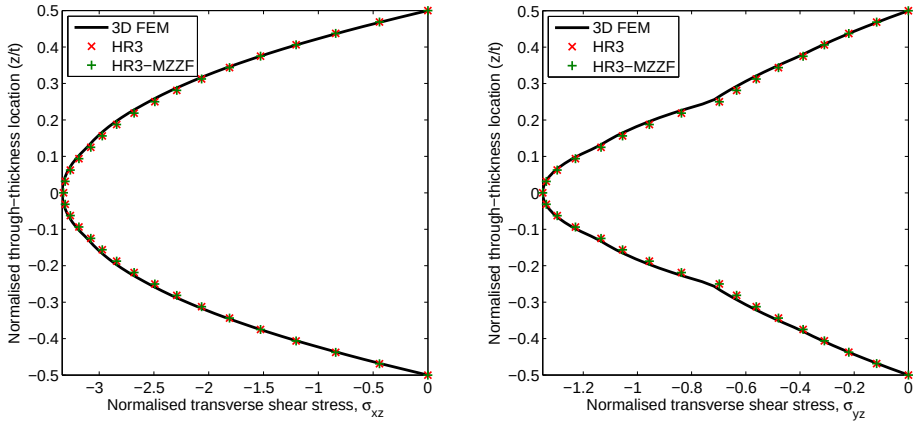


**(a)** Normalised transverse shear stress, $\bar{\sigma}_{xz}$ **(b)** Normalised transverse shear stress, $\bar{\sigma}_{yz}$

**Figure 41:** Laminate VAT C: Through-thickness distributions of the normalised transverse shear stresses ($\bar{\sigma}_{xz}$ and $\bar{\sigma}_{yz}$) at $(a/4, b/2, z)$ and $(a/2, b/4, z)$, respectively for $a/t = 10$.

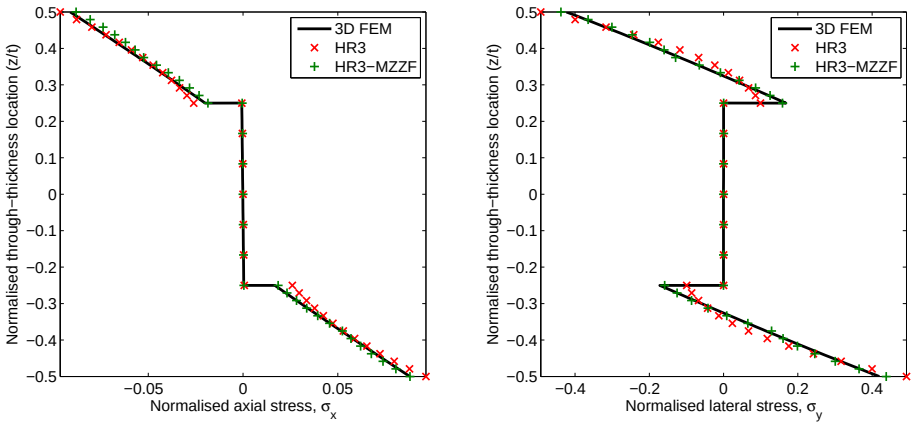


**(a)** Normalised axial stress, $\bar{\sigma}_x$ **(b)** Normalised lateral stress, $\bar{\sigma}_y$

**Figure 42:** Laminate VAT D: Through-thickness distributions of the normalised axial ($\bar{\sigma}_x$) and lateral ($\bar{\sigma}_y$) stresses at $(a/2, b/2, z)$ for $a/t = 10$.

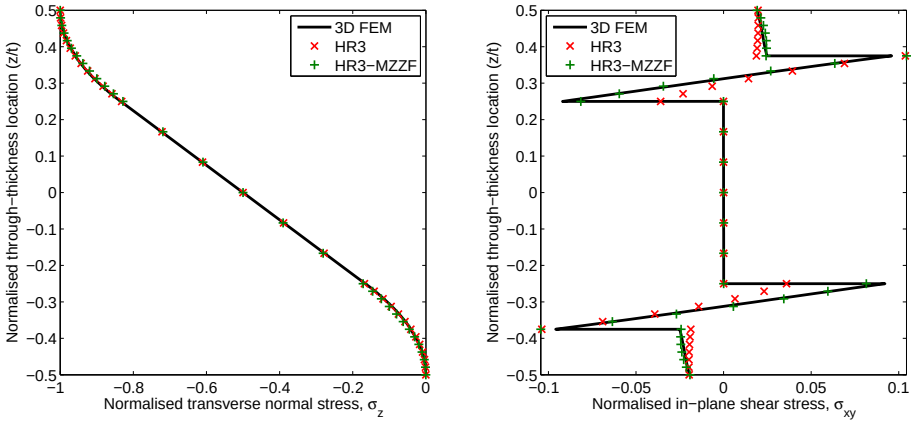


**(a)** Normalised transverse normal stress, $\bar{\sigma}_z$ **(b)** Normalised in-plane shear stress, $\bar{\sigma}_{xy}$

**Figure 43:** Laminate VAT D: Through-thickness distributions of the normalised transverse normal ($\bar{\sigma}_z$) and in-plane shear ($\bar{\sigma}_{xy}$) stresses at $(a/2, b/2, z)$ and $(a/4, b/4, z)$, respectively for $a/t = 10$.

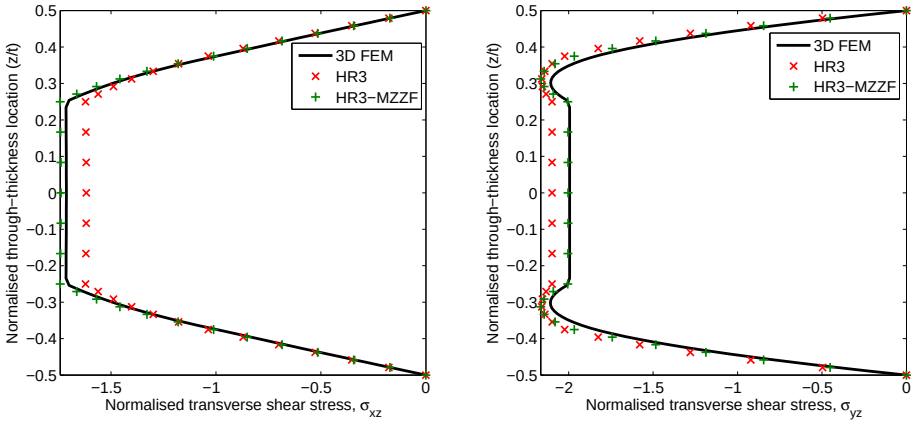


**(a)** Normalised transverse shear stress, $\bar{\sigma}_{xz}$ **(b)** Normalised transverse shear stress, $\bar{\sigma}_{yz}$

**Figure 44:** Laminate VAT D: Through-thickness distributions of the normalised transverse shear stresses ($\bar{\sigma}_{xz}$ and $\bar{\sigma}_{yz}$) at $(a/4, b/2, z)$ and $(a/2, b/4, z)$, respectively for $a/t = 10$.

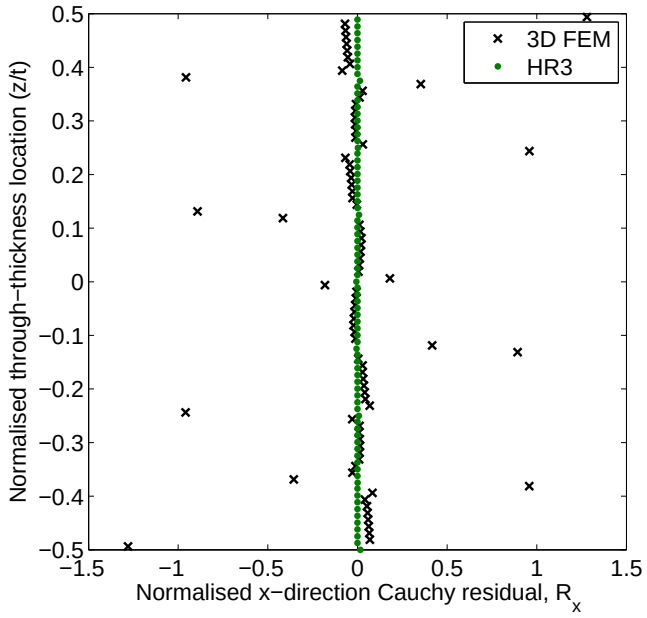


**(a)** Normalised $x$-direction Cauchy residual, $\bar{R}_x$

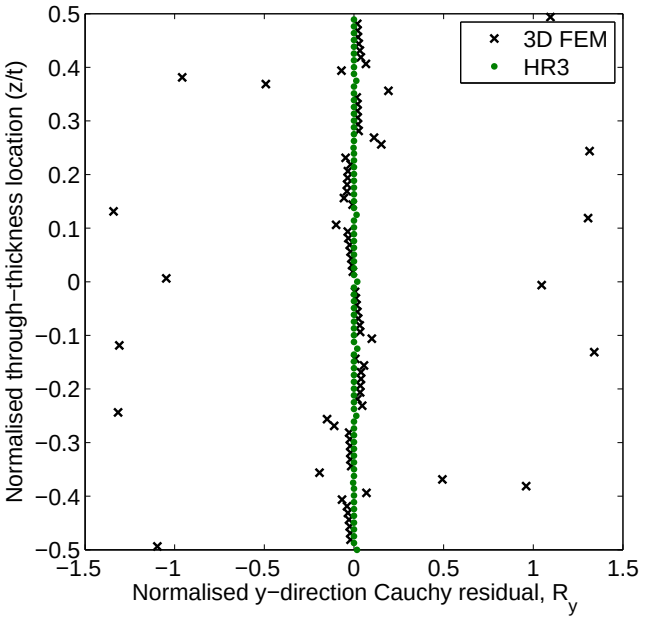


**(b)** Normalised $y$-direction Cauchy residual, $\bar{R}_y$

**Figure 45:** Laminate VAT B: Normalised $x$-direction and $y$-direction Cauchy residuals $\bar{R}_x$ and $\bar{R}_y$, respectively, for 3D FEM and HR models at $(a/4, b/4, z)$ for $a/t = 10$.

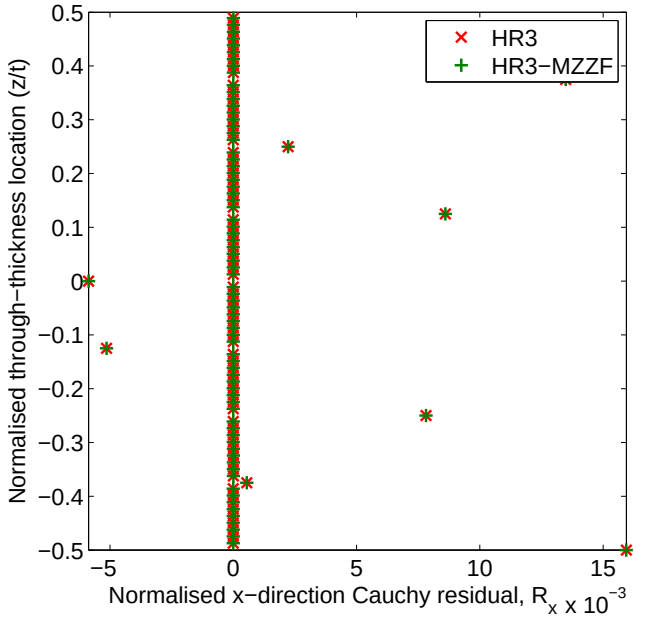


**(a)** Normalised $x$-direction Cauchy residual, $\bar{R}_x$

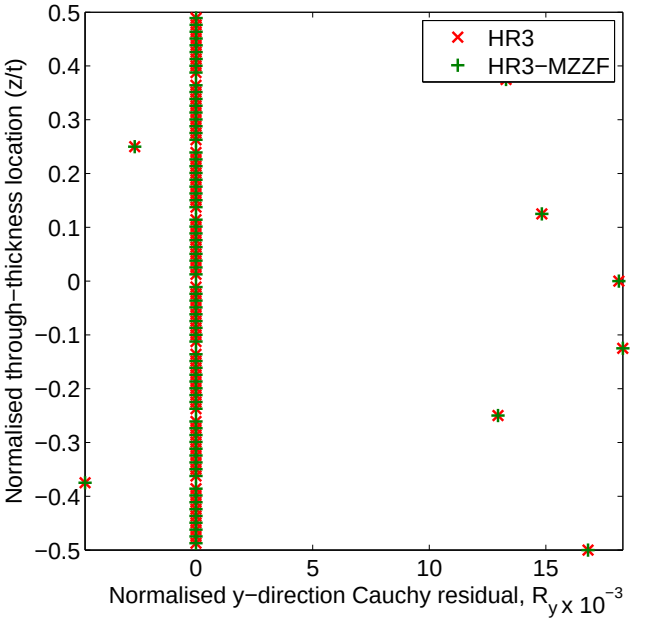


**(b)** Normalised $y$-direction Cauchy residual, $\bar{R}_y$

**Figure 46:** Laminate VAT B: Normalised $x$-direction and $y$-direction Cauchy residuals $\bar{R}_x$ and $\bar{R}_y$, respectively, for all HR models at $(a/4, b/4, z)$ for $a/t = 10$.

As a result, we observe that very detailed 3D FEM meshes with more than ten elements per layer and multiple hours of runtime, do not guarantee that Cauchy's equilibrium equations are satisfied with negligible error. The HR formulation presented herein predicts 3D stress fields that equilibrate more accurately than 3D FEM. At the same time, the HR models reduce the number of variables by four orders of magnitude when analysing variable-stiffness laminates, which leads to a reduction in run-time from 10 hours in Abaqus on a high-performance computer with 128 GB of RAM to 1-2 minutes on a standard desktop PC running interpreted MATLAB.

This combination of accuracy and computational expense makes the HR formulation an attractive basis for industrial design tools. Two important reasons for the performance of the HR models is their mixed displacement- and stress-based nature, which inherently satisfies the equilibrium of stresses in a variational sense, compared to the displacement-based 3D FEM model in Abaqus, which only explicitly guarantees the compatibility of displacements and strains. Second, the strong-form DQM solution technique used herein allows more accurate computation of derivatives and enforces both essential and natural boundary conditions explicitly.

## 4. Conclusions

Using the 2D ESLT derived from the HR principle in *Part I* of this work [1], a large and diverse set of straight-fibre and variable-stiffness composite and sandwich beams has been analysed under different bending load cases, boundary conditions and thickness to characteristic length ratios. The laminates considered here include a variety of symmetric and non-symmetric, balanced and unbalanced, multimaterial sandwich plates, as well as laminates with *3D heterogeneity*, i.e. laminates with material properties that vary in all three dimensions.

Stress fields for orthotropic straight-fibre laminates were validated against 3D elasticity solutions, whereas the anisotropic straight-fibre and variable-stiffness laminates were compared against 3D FEM results. Overall, the through-thickness stress fields of the HR model show excellent correlation to approximately 2% of 3D elasticity and 3D FEM results for characteristic length to thickness ratios of $10:1$. Below this value, agreement to approximately 5% was found for characteristic length to thickness ratios as small as $5:1$. In some applications, e.g. wind turbine blade roots, where the characteristic length to thickness may approach values of $5:1$, transverse normal deformation becomes increasingly significant. The accuracy of the HR model, combined with the three-order-of-magnitude reduction in runtime compared to high-fidelity 3D FEM models, makes the HR formulation well-suited for industrial design tools.

The results in Section 2.1.2 show that the HR3-RZTmx model, i.e. using the RZT ZZ function accounting for EWLs, correlates most accurately with Pagano's 3D elasticity solution for orthotropic straight-fibre laminates. Thus, Gherlone's adaptation [33] of the RZT ZZ function is recommended to obtain most accurate stress results. The HR model using MZZF (HR3-MZZF) is also accurate for simple sandwich laminates comprising stiff face layers and a soft core. When two different cores or three unique material properties are used within a laminate, MZZF results in large errors. This discrepancy occurs because MZZF is based on an arbitrary ad hoc assumption of the ZZ slope changes between layers, and not on actual material properties like the RZT ZZ function. For non-sandwich laminates, the HR3 model without ZZ functionality gives similar accuracy to the HR3-RZTmx and HR3-MZZF models, and as a result of the reduced computational expense, is the preferred option for typical non-sandwich composite laminates used in engineering applications.

The anisotropic laminates in Section 2.2.2 are influenced less by the ZZ effect as the layerwise differences in transverse shear moduli is reduced for combinations of off-axis layers compared to orthotropic 0/90 laminates. Furthermore, the results for anisotropic, straight-fibre laminates confirm that the HR3-RZTmx model predicts the 3D stress fields most accurately for general multimaterial laminations, where layer material properties may vary by orders of magnitude. However, for the variable-stiffness plates studied in Section 3.1, the RZT ZZ function leads to ill-conditioning of the numerical DQM stiffness matrix due to local singularities in the in-plane derivatives of the RZT ZZ function. Thus, within the present global DQM framework, the HR3-RZTmx is not suited for robust analysis of variable-stiffness laminates. To remedy this problem, a local DQM approach, where only a small number of grid points rather than the full domain is used to compute derivatives, should be tested. Alternatively, a strong-form or weak-form FEM that assigns constant fibre-angles to each element within the discretisation mesh would also remove the numerical ill-conditioning.

The results presented in Sections 2.2.2 and 3.1 suggest that the 3D stress fields from the HR models satisfy Cauchy's 3D equilibrium equations more accurately, and at a three-order degree of freedom reduction in computational cost, compared to high-fidelity 3D FEM models in Abaqus. This point highlights an important advantage of the HR variational statement: it is computationally more efficient to enforce the equilibrium of stresses explicitly in a variational sense than relying on the assumption that finer discretisation meshes in displacement-based theories converge to a negligible residual. The largest errors between the present HR plate model and the 3D FEM results, for both straight-fibre and tow-steered composites, occur for the in-plane shear stress $\sigma_{xy}$. To date, the authors have not been able to elucidate the origin of this bias towards the in-plane shear stress accuracy, and this issue is to be investigated further in future work.

Indeed, the results show that a third-order HR model enhanced by the RZT ZZ function can robustly model

straight-fibre composites and sandwich panels with layer properties that vary by multiple orders of magnitude. Previously, the consensus in the literature was that accurate 3D stress fields for such laminates can only be predicted using layerwise theories. As a 2D ESLT, the HR model is not capable of enforcing unique boundary conditions for different layers. However, these loading conditions are rare in practical engineering structures where the interface between different components typically involves the entire cross-section. Hence, the present work questions the necessity of using layerwise theories for practical engineering structures, and suggests that future work should re-examine when these approaches are worth their extra computational effort.

## Acknowledgments

This work was supported by the Engineering and Physical Sciences Research Council through the EPSRC Centre for Doctoral Training in Advanced Composites [grant number EP/G036772/1] at the University of Bristol.

## References

[1] RMJ Groh and PM Weaver. A Hellinger-Reissner-type equivalent single-layer theory for heterogeneous laminated plates. Part I: Model formulation. *Submitted for publication*.

[2] AAG Cooper. *Trajectorial fiber reinforcement of composite structures*. PhD thesis, Department of Mechanical and Aerospace Engineering, Washington University, 1972.

[3] MW Hyer and HH Lee. The use of curvilinear fiber format to improve buckling resistance of composite plates with central circular holes. *Composite Structures*, 18:239–261, 1991.

[4] MW Hyer and RF Charette. The use of curvilinear fiber format in composite structure design. *AIAA Journal*, 29(6):1011–1015, 1991.

[5] Z Gurdal and R Olmedo. In-plane response of laminates with spatially varying fiber orientations: Variable stiffness concept. *AIAA Journal*, 31(4):751–758, 1993.

[6] Z Gurdal, BF Tatting, and CK Wu. Variable stiffness composite panels: Effects of stiffness variation on the in-plane and buckling response. *Composites Part A: Applied Science and Manufacturing*, 39:911–922, 2008.

[7] S Setoodeh, MM Abdalla, ST Ijsselmuiden, and Z Gurdal. Design of variable stiffness composite panels for maximum buckling load. *Composite Structures*, 87:109–117, 2008.

[8] PM Weaver, KD Potter, K Hazra, MAR Saverymuthapulle, and MT Hawthorne. Buckling of variable angle tow plates: From concept to experiment. In *Proceedings of the 50th AIAA/ASME/ASCE/AHS/ASC Structures, Structural Dynamics, and Materials Conference*, Palm Springs, California, USA, 2009.

[9] CS Lopes, Z Gurdal, and PP Camanho. Tailoring for strength of composite steered-fibre panels with cutouts. *Composites Part A: Applied Science and Manufacturing*, 41:1760–1767, 2010.

[10] Z Wu, PM Weaver, G Raju, and BC Kim. Buckling analysis and optimisation of variable angle tow composite plates. *Thin-Walled Structures*, 60:163–172, 2012.

[11] G Raju, Z Wu, BC Kim, and PM Weaver. Prebuckling and buckling analysis of variable angle tow plates with general boundary conditions. *Composite Structures*, 94(9):2961–2970, 2012.

[12] W Liu and R Butler. Buckling optimization of variable-angle-tow panels using the infinite-strip method. *AIAA Journal*, 51:1442–1449, 2013.

[13] G Raju, Z Wu, and PM Weaver. Buckling and postbuckling of variable angle tow composite plates under in-plane shear loading. *International Journal of Solids and Structures*, 58:270–287, 2015.

[14] Z Wu, G Raju, and PM Weaver. Postbuckling analysis of variable angle tow composite plates. *International Journal of Solids and Structures*, 50:1770–1780, 2013.

[15] JP Peterson, P Seide, and VI Weingarten. Buckling of thin-walled circular cylinders. Technical Report NASA-SP-8007, NASA, 1968.

[16] SC White and PM Weaver. Towards imperfection insensitive buckling response of shell structures shells with plate-like post-buckled responses. In *Proceedings of the 4th Aircraft Structural Design Conference of the Royal Aeronautical Society*, Belfast, UK, 2014.

[17] SC White and PM Weaver. Bend-free shells under uniform pressure with variable-angle tow derived anisotropy. *Composite Structures*, 94(11):3207–3214, 2012.

[18] A Beakou, M Cano, J-B Le Cam, and V Verney. Modelling slit tape buckling during automated prepreg manufacturing: A local approach. *Composite Structures*, 93:2628–2635, 2011.

[19] BC Kim, K Potter, and PM Weaver. Continuous tow shearing for manufacturing variable angle tow composites. *Composites Part A: Applied Science and Manufacturing*, 43(8):1347–1356, 2012.

[20] BC Kim, PM Weaver, and K Potter. Manufacturing characteristics of the continuous tow shearing method for manufacturing of variable angle tow composites. *Composites Part A: Applied Science and Manufacturing*, 61(8):141–151, 2014.

[21] H Akhavan and P Ribeiro. Natural modes of vibration of variable stiffness composite laminates with curvilinear fibers. *Composite Structures*, 93:3040–3047, 2011.

[22] H Akhavan, P Ribeiro, and MFSF Moura. Large deflection and stresses in variable stiffness composite laminate with curvilinear fibres. *International Journal of Mechanical Sciences*, 73:14–26, 2013.

[23] RMJ Groh and PM Weaver. Static inconsistencies in certain axiomatic higher-order shear deformation theories for beams, plates and shells. *Composite Structures*, 120:231–245, 2015.

[24] H Akhavan and P Ribeiro. Non-linear vibrations of variable stiffness composite laminated plates. *Composite Structures*, 94:2424–2432, 2012.

[25] BH Coburn, Z Wu, and PM Weaver. Buckling analysis of stiffened variable angle tow panels. *Composite Structures*, 111:259–270, 2014.

[26] BH Coburn, Z Wu, and PM Weaver. Buckling analysis and optimization of blade stiffened variable stiffness panels. In *Proceedings of the 56th AIAA/ASME/ASCE/AHS/ASC Structures, Structural Dynamics and Materials Conference*, number 1438, Kissimmee, Florida, USA, 2015.

[27] AH Akbarzadeh, M Arian Nik, and D Pasini. The role of shear deformation in laminated plates with curvilinear fiber paths and embedded defects. *Composite Structures*, 118:217–227, 2014.

[28] RMJ Groh, PM Weaver, SC White, G Raju, and Z Wu. A 2D equivalent single-layer formulation for the effect of transverse shear on laminated plates with curvilinear fibres. *Composite Structures*, 100:464–478, 2013.

[29] S Yazdani and P Ribeiro. A layerwise p-version finite element formulation for free vibration analysis of thick composite laminates with curvilinear fibres. *Composite Structures*, 120:531–542, 2015.

[30] S Yazdani, P Ribeiro, and JD Rodrigues. A p-version layerwise model for large deflection of composite plates with curvilinear fibres. *Composite Structures*, 108:181–190, 2014.

[31] F Tornabene, N Fantuzzi, M Bacciocchi, and E Viola. Higher-order theories for the free vibrations of doubly-curved laminated panels with curvilinear reinforcing fibers by means of a local version of the GDQ method. *Composites Part B: Engineering*, 81:196–230, 2015.

[32] A Tessler, M Di Sciuva, and M Gherlone. Refined zigzag theory for laminated composite and sandwich plates. Technical Publi-

cation 215561, National Aeronautics and Space Administration, 2009.

[33] M Gherlone. On the use of zigzag functions in equivalent single layer theories for laminated composite and sandwich beams: A comparative study and some observations on external weak layers. *Journal of Applied Mechanics*, 80:1–19, 2013.

[34] RMJ Groh. *Non-classical effects in straight-fibre and tow-steered composite beams and plates*. PhD thesis, University of Bristol, 2015.

[35] NJ Pagano. Exact solutions for rectangular bidirectional composites and sandwich plates. *Journal of Composite Materials*, 4(20):20–34, 1970.

[36] RMJ Groh and PM Weaver. On displacement-based and mixed-variational equivalent single layer theories for modelling highly heterogeneous laminated beams. *International Journal of Solids and Structures*, 59:147–170, 2015.

[37] A Toledano and H Murakami. A composite plate theory for arbitrary laminate configurations. *Journal of Applied Mechanics*, 54(1):181–189, 1987.

[38] R Bellman, G Kashef, and J Casti. Differential quadrature: A technique for the rapid solution of nonlinear partial differential equations. *Journal of Computational Physics*, 10:40–52, 1972.

[39] C Shu and BE Richards. High resolution of natural convection in a square cavity by generalized differential quadrature. In *Proceedings of the 3rd International Conference on Advances in Numerical Methods in Engineering, Theory and Applications*, pages 978–985, Swansea, UK, 1990.

[40] C Shu and BE Richards. Application of generalized differential quadrature to solve two-dimensional incompressible Navier-Stokes equations. *International Journal for Numerical Methods in Fluids*, 15:791–798, 1992.

[41] JR Quan and CT Chang. New insights in solving distributed system equations by the quadrature method – I. Analysis. *Computers & Chemical Engineering*, 13(7):779–788, 1989.

[42] C Shu. *Differential Quadrature and its Application in Engineering*. Springer Verlag, 1st edition, 2000.

[43] F Tornabene, N Fantuzzi, F Ubertini, and E Viola. Strong formulation finite element method based on differential quadrature: A survey. *Applied Mechanics Reviews*, 67:1–55, 2015.

[44] C Shu and H Du. A generalized approach for implementing general boundary conditions in the GDQ free vibration analysis of plates. *International Journal of Solids and Structures*, 34(7):837–846, 1997.

[45] E Cheney and D Kincaid. *Numerical Mathematics and Computing*. Cengage Learning, 6th edition, 2007.

[46] K Levenberg. A method for the solution of certain non-linear problems in least squares. *Quarterly of Applied Mathematics*, 2:164–168, 1944.

[47] D Marquardt. An algorithm for least-squares estimation of nonlinear parameters. *SIAM Journal on Applied Mathematics*, 11(2):431–441, 1963.

[48] SC White, G Raju, and PM Weaver. Initial post-buckling of variable-stiffness curved panels. *Journal of the Mechanics and Physics of Solids*, 71:132–155, 2014.

[49] RMJ Groh and PM Weaver. Buckling analysis of variable angle tow, variable thickness panels with transverse shear effects. *Composite Structures*, 107:482–493, 2014.